BIOCHEMISTRY

RNA G-quadruplex organizes stress granule assembly through DNAPTP6 in neurons

Sefan Asamitsu[1,2]†*, Yasushi Yabuki[1,3]†, Kazuya Matsuo[1], Moe Kawasaki[1,3], Yuki Hirose[4], Gengo Kashiwazaki[5], Anandhakumar Chandran[6]‡, Toshikazu Bando[4], Dan Ohtan Wang[2,7], Hiroshi Sugiyama[4,8], Norifumi Shioda[1,3]*

Consecutive guanine RNA sequences can adopt quadruple-stranded structures, termed RNA G-quadruplexes (rG4s). Although rG4-forming sequences are abundant in transcriptomes, the physiological roles of rG4s in the central nervous system remain poorly understood. In the present study, proteomics analysis of the mouse forebrain identified DNAPTP6 as an RNA binding protein with high affinity and selectivity for rG4s. We found that DNAPTP6 coordinates the assembly of stress granules (SGs), cellular phase-separated compartments, in an rG4-dependent manner. In neurons, the knockdown of DNAPTP6 diminishes the SG formation under oxidative stress, leading to synaptic dysfunction and neuronal cell death. rG4s recruit their mRNAs into SGs through DNAPTP6, promoting RNA self-assembly and DNAPTP6 phase separation. Together, we propose that the rG4-dependent phase separation of DNAPTP6 plays a critical role in neuronal function through SG assembly.

INTRODUCTION

RNA secondary structures play multifaceted physiological functions, including roles in translation processes, mRNA decay, inflammation responses, and evolutionary survival of RNA viruses (1–4). Consecutive guanine RNA sequences can adopt quadruple-stranded structures, termed RNA G-quadruplexes (rG4s), particularly in the presence of potassium cations. rG4s are considered to have peculiar implications for RNA metabolism (5, 6), owing to the unique thermodynamic property (7), structural features (8), and interacting biomolecules (9, 10). The number of rG4-forming sequences has been predicted to be 3800 in about 2300 different gene transcripts of HeLa cells (11). rG4-forming sequences within mRNAs are relatively enriched in the 5′ untranslated region (5′UTR) and the 3′UTR compared with the coding sequence (CDS) (11). Cellular G4 structures tend to be unfolded by RNA helicases or recognized by rG4-binding proteins (rG4BPs) (12) and are transiently folded by small molecules (13–15) or the reduction of RNA helicases (16, 17). Some of the rG4s have been proven to be involved in intracellular phenomena, including stress responses (16, 18, 19) and the inhibition of ribosome scanning (13), and can be used as marks for upstream open reading frames in certain sets of genes (17, 20). However, the functions of most rG4s throughout the transcriptome remain unknown.

Aberrant rG4 formation is associated with neurodegenerative diseases (9, 21). rG4s formed by excessive GGGGCC repeat RNA sequences in C9orf72 result in the formation of phase-separated aggregates in neurons, which is considered a pathogenic factor in C9orf72 amyotrophic lateral sclerosis and frontotemporal dementia (18, 21–23). Recently, our group has reported that rG4s formed by excessive CGG repeat RNA sequences at FMR1 induce liquid-to-solid phase transition of condensates of FMRpolyG, a major pathogenic protein (24). This transition produces insoluble inclusions in neurons and leads to neuronal dysfunction observed in fragile X-related tremor/ataxia syndrome (24). Despite neuropathological features of rG4s, the physiological roles of rG4s in the central nervous system remain largely unclear.

In this study, we showed that rG4s and an rG4BP, DNAPTP6, coordinate the assembly of stress granules (SGs), cytoplasmic membrane-less compartments driven by liquid-liquid phase separation (LLPS). DNAPTP6 can preferentially bind to rG4s and promote SG assembly via rG4-dependent phase separation, in which rG4s themselves have a strong ability to undergo RNA phase separation and enhance DNAPTP6 phase separation. In biological analysis and bioinformatics, we found that mRNAs containing multiple rG4s are significantly enriched in SGs. Impairment of rG4-dependent phase separation via DNAPTP6 knockdown perturbed SG formation, which led to synaptic dysfunction and neuronal cell death. Our findings provide an insight into the role of rG4-dependent phase separation and functional SG assembly in neurons.

[1]Department of Genomic Neurology, Institute of Molecular Embryology and Genetics (IMEG), Kumamoto University, Kumamoto, Japan. [2]Center for Biosystems Dynamics Research (BDR), RIKEN, Kobe, Japan. [3]Graduate School of Pharmaceutical Sciences, Kumamoto University, Kumamoto, Japan. [4]Department of Chemistry, Graduate School of Science, Kyoto University, Kyoto, Japan. [5]Major in Advanced Bioscience, Graduate School of Agriculture, Kindai University, Nara, Japan. [6]Ludwig Cancer Research Oxford, University of Oxford, Old Road Campus Research Building, Oxford, UK. [7]Graduate School of Biostudies, Kyoto University, Kyoto, Japan. [8]Institute for Integrated Cell-Material Science (WPI-iCeMS), Kyoto University, Sakyo, Kyoto, Japan.
*Corresponding author. Email: sefan.asamitsu@riken.jp; shioda@kumamoto-u.ac.jp
†These authors contributed equally to this work.
‡Present address: Discovery Technology and Genomics, Novo Nordisk Research Centre Oxford, Novo Nordisk Ltd., Oxford, UK.

RESULTS

Identification of an rG4BP expressed in neurons, DNAPTP6

First, we performed proteomic screening to search for rG4BPs using liquid chromatography–tandem mass spectrometry (LC-MS/MS) on pulled-down samples from lysates of adult mouse forebrain with a G4-specific antibody (BG4) (Fig. 1A) (25, 26). BG4 is a single chain FV antibody specifically recognizing G4 structures in DNAs and RNAs, and is used for biochemical studies including
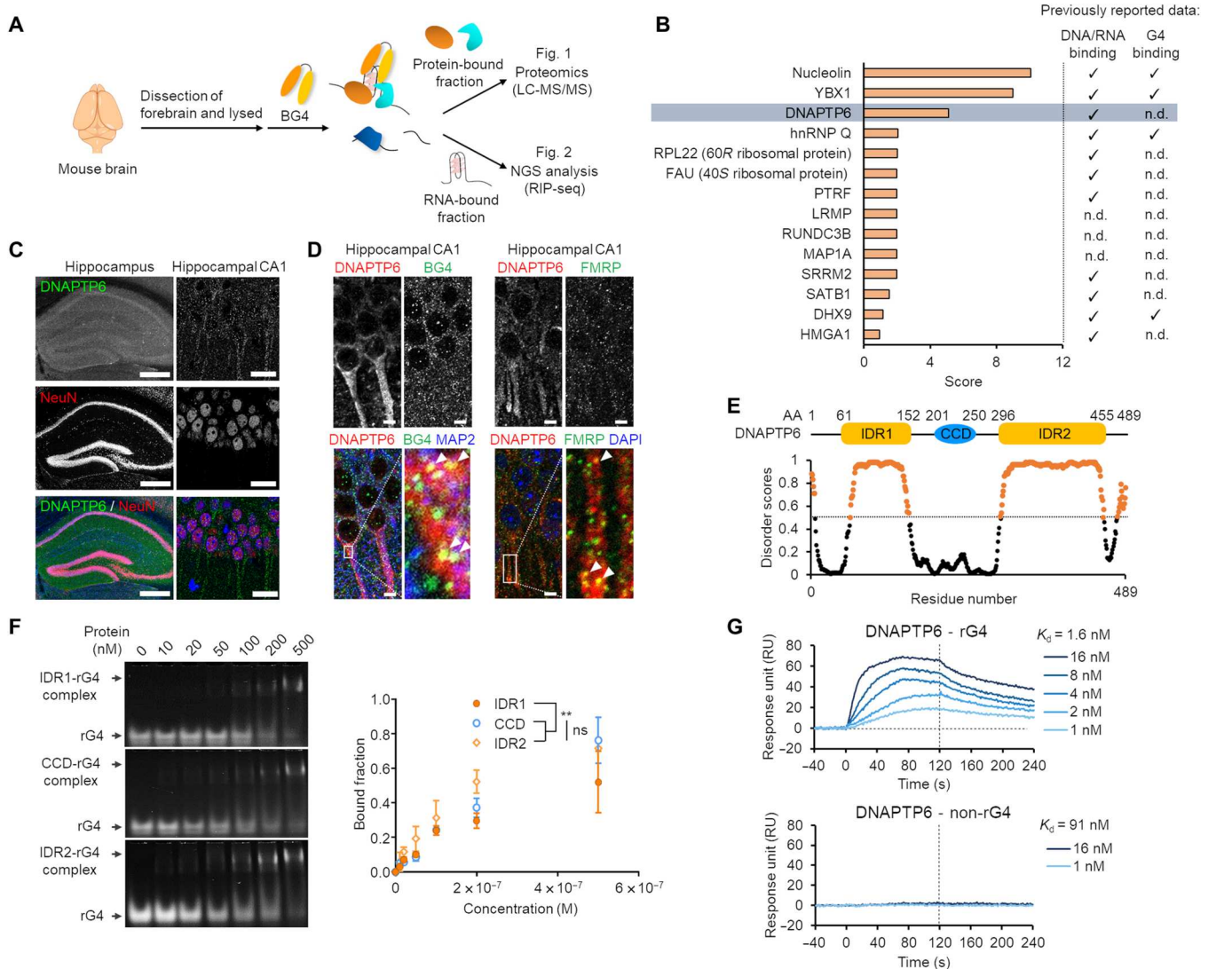
Fig. 1. DNAPTP6 is a neuronal rG4-binding protein. (**A**) Schematic for immunoprecipitation by BG4 to identify G4BPs and rG4s in mouse forebrain tissue. (**B**) Proteins obtained from the LC-MS/MS analysis. n.d., not determined. (**C**) Representative confocal images showing the distribution of endogenous DNAPTP6 in mouse hippocampus (left) and a hippocampal CA1 region (right). NeuN was visualized as the neuronal marker. Scale bars, 250 μm (left) and 20 μm (right). (**D**) Representative confocal images showing the subcellular distribution of DNAPTP6 in the hippocampal CA1 region. FMRP was visualized as the neuronal granule marker in the cytoplasm and dendrites. Arrowheads point to regions of colocalization. Scale bars, 5 μm. (**E**) Characteristic domains of DNAPTP6. IDRs were predicted by DISOPRED3. AA, amino acid. (**F**) EMSA for the interaction of each domain of DNAPTP6 with a typical rG4 oligomer (TERRA) labeled with FAM at the 5′ end. ns, not significant; **$P < 0.01$ (two-way ANOVA with Bonferroni's multiple comparison test); $n = 2$ from two independent experiments. (**G**) SPR sensorgrams for the interaction of recombinant DNAPTP6 with rG4 (TERRA) and its mutant that is unable to form rG4 (mTERRA, non-rG4). Error bars represent SD.

immunochemistry (26, 27) and immunoprecipitation experiments (28, 29), to detect rG4s. LC-MS/MS analysis revealed that well-documented G4BPs, Nucleolin (30), hnRNPQ (31), DHX9 (17), and YBOX1 (32), had high scores, confirming the successful enrichment of G4BPs (Fig. 1B). Among the top 13 proteins, we focused on DNAPTP6 because it had the highest score among proteins unidentified as rG4BPs.

DNAPTP6 is reported to be involved in ribosomal biogenesis and translation in response to oxidative stress in human skeletal myoblasts (33). However, its cellular function in the central nervous system remains unclear. We examined the distribution of DNAPTP6 in the adult mouse brain via immunohistochemical

analysis. We found that DNAPTP6 was expressed in neuronal marker NeuN–positive cells, as shown in the hippocampal CA1 region (Fig. 1C). DNAPTP6 was substantially observed as granule-like structures in the cytoplasm and neuronal dendrites and colocalized with BG4-positive foci and FMRP-positive granules (Fig. 1D, arrowheads), suggesting that DNAPTP6 is a component of RNA granules that contain rG4s in the brain.

DISOPRED3 (34) analysis predicted that DNAPTP6 has two intrinsically disordered regions (IDRs: IDR1 and IDR2), with a coiled-coil domain (CCD) between them (Fig. 1E). To determine the role of each domain of DNAPTP6 in subcellular granule formation, we transfected mouse neuroblastoma Neuro-2A cells with

plasmids encoding green fluorescent protein (GFP)–tagged full-length DNAPTP6 (GFP-FL) and its deletion mutants, GFP-ΔIDR1, GFP-ΔCCD, and GFP-ΔIDR2 (fig. S1A). We confirmed that GFP-FL exists as granules in the cytoplasm in Neuro-2A cells (fig. S1B), similar to that in adult mouse hippocampi (Fig. 1D). Although GFP-ΔIDR1 was present in a granular form similar to GFP-FL, GFP-ΔIDR2 and GFP-ΔCCD existed in a more diffused state, as evidenced by the lower inhomogeneity of their cytoplasmic distribution (fig. S1, C to F).

To identify the protein domains responsible for rG4-binding capability, we divided DNAPTP6 into three segments containing IDR1, CCD, and IDR2 and then purified each SUMO-tagged protein for an electrophoresis mobility shift assay (EMSA). All segments showed a binding affinity to a typical rG4 (TERRA, 5′-UUA GGGUUAGGGUUAGGGUUAGGG-3′); especially, SUMO-CCD and SUMO-IDR2 showed a significant rG4 affinity (Fig. 1F and fig. S2).

To precisely determine whether DNAPTP6 selectively interacts with rG4s, we performed quantitative surface plasmon resonance (SPR)–binding assays using recombinant full-length DNAPTP6 and two RNA oligomers: TERRA (rG4) and its mutant that is unable to form rG4s, mTERRA (non-rG4, 5′-UUACCGUUACCG UUACCGUUACCG-3′). Biotinylated TERRA or mTERRA was immobilized onto a streptavidin-coated sensor chip, and solutions of recombinant DNAPTP6 with a series of concentrations were injected. The SPR signals in the buffer containing 100 mM KCl were then measured to obtain kinetic parameters (k_{on} and k_{off}) and dissociation constants (K_d). We found that DNAPTP6 showed a much higher selectivity (57-fold) to TERRA compared with mTERRA (Fig. 1G and fig. S3). We also confirmed by EMSA that DNAPTP6 has a preferential binding affinity to rG4s over other characteristic secondary structures of nucleic acids (fig. S4). Collectively, these findings suggest that DNAPTP6 is an rG4BP with structure selectivity and its CCD and IDR2 domains are primarily involved in the rG4 selectivity and intracellular granule formation.

Comprehensive analysis of rG4-forming mRNAs in mouse forebrain

Next, we analyzed BG4-bound mRNAs via RNA immunoprecipitation coupled with sequencing (BG4 RIP-seq) (Fig. 1A). We compared fragments per kilobase of exon per million mapped reads (FPKM) obtained from BG4-enriched fractions with those from immunoglobulin G (IgG)–treated fractions to identify mRNAs containing G4 structures in adult mouse forebrain tissues (Fig. 2A). In the prediction of quadruplex-forming guanine-rich sequences (QGRS) mapper (35), all BG4-enriched mRNAs (P value cutoff: 0.05) were found to have putative rG4-forming sequences with two or three G-tetrad layers (Fig. 2A, fig. S5A, and table S1). Successful enrichment of rG4-forming RNAs was further confirmed by the fact that the guanine-cytosine contents of the BG4-bound mRNAs were significantly higher than those of randomly sampled transcripts (fig. S5B). We found that relatively rigid rG4s (which have three G-tetrads) were primarily distributed in the 3′UTR (fig. S5, C to E), in agreement with the previously reported trend for the distribution of rG4-forming sequences in human transcripts (11). Twenty-three percent and 9% of the BG4-enriched mRNAs overlapped with rG4 transcriptomes identified in mouse embryonic stem cells and Hela cells, respectively (fig. S5, F and G).

Among BG4-bound mRNAs in the forebrain, *Mark2*, *Stxbp5*, *Limd2*, and *Dazap1* have multiple rG4-forming sequences that can likely form three G-tetrads in the 5′ and 3′UTRs (Fig. 2B and fig. S5A). The *Mark2* and *Stxbp5* mRNAs that are the most G4-rich mRNAs were further analyzed using other algorithms, such as consecutive G over consecutive C ratio (cGcC), G4Hunter (G4H), and G4 Neural Network (G4NN), provided by the G4RNA screener (36). We confirmed that the region of rG4-forming sequences predicted by the QGRS mapper also displayed high G4 scores with the G4RNA screener (Fig. 2C and fig. S6).

To investigate whether these predicted rG4-forming sequences are truly folded into G4 structures, we performed a series of biophysical assays using *Mark2* RNA oligomers (M1, M2, M3, and M4) and *Stxbp5* RNA oligomers (S1, S2, and S3). In G4-stabilizing 100 mM KCl conditions, the circular dichroism (CD) spectra of M1, M2, and M4 gave a substantial positive absorption band at 262 nm, a shallow negative band at 240 nm, and a positive band at 210 nm, which are typical features of parallel type G4 structures (Fig. 2D and fig. S7, A and B). Conversely, under G4-nonstabilizing 100 mM LiCl conditions, the entire spectral status changed, and the typical features were not observed, suggesting the conversion into unstructured forms (Fig. 2D and fig. S7, A and B). To further confirm G4 folding on these RNA oligomers, we assessed cation-dependent RNA thermal denaturing property by measuring the RNA melting temperature (T_m). M1, M2, and M4 exhibited much higher thermal stability under KCl conditions than under LiCl conditions (Fig. 2E and fig. S7, C and D), indicating specific thermal stabilization of G4 structures by K+ cations.

To determine which guanine residues participate in G-tetrads, we performed ribonuclease (RNase) T1 footprinting assays. When an RNA sequence is folded into a G4 structure, RNase T1 cleaves selectively free guanine residues or ones situated at the loop region, whereas guanine residues participating in G-tetrads are partially protected from RNase T1 cleavage (23). For M2 under 100 mM KCl conditions, the entire RNase T1 cleavage pattern was weaker than that under 100 mM LiCl conditions (Fig. 2F). The cleaved and protected status relative to that under 100 mM LiCl provided some detailed structural information (Fig. 2G). The same experiments were performed for M1 and M4, and we were able to determine guanine residues participating in G-tetrads (fig. S7, E and F).
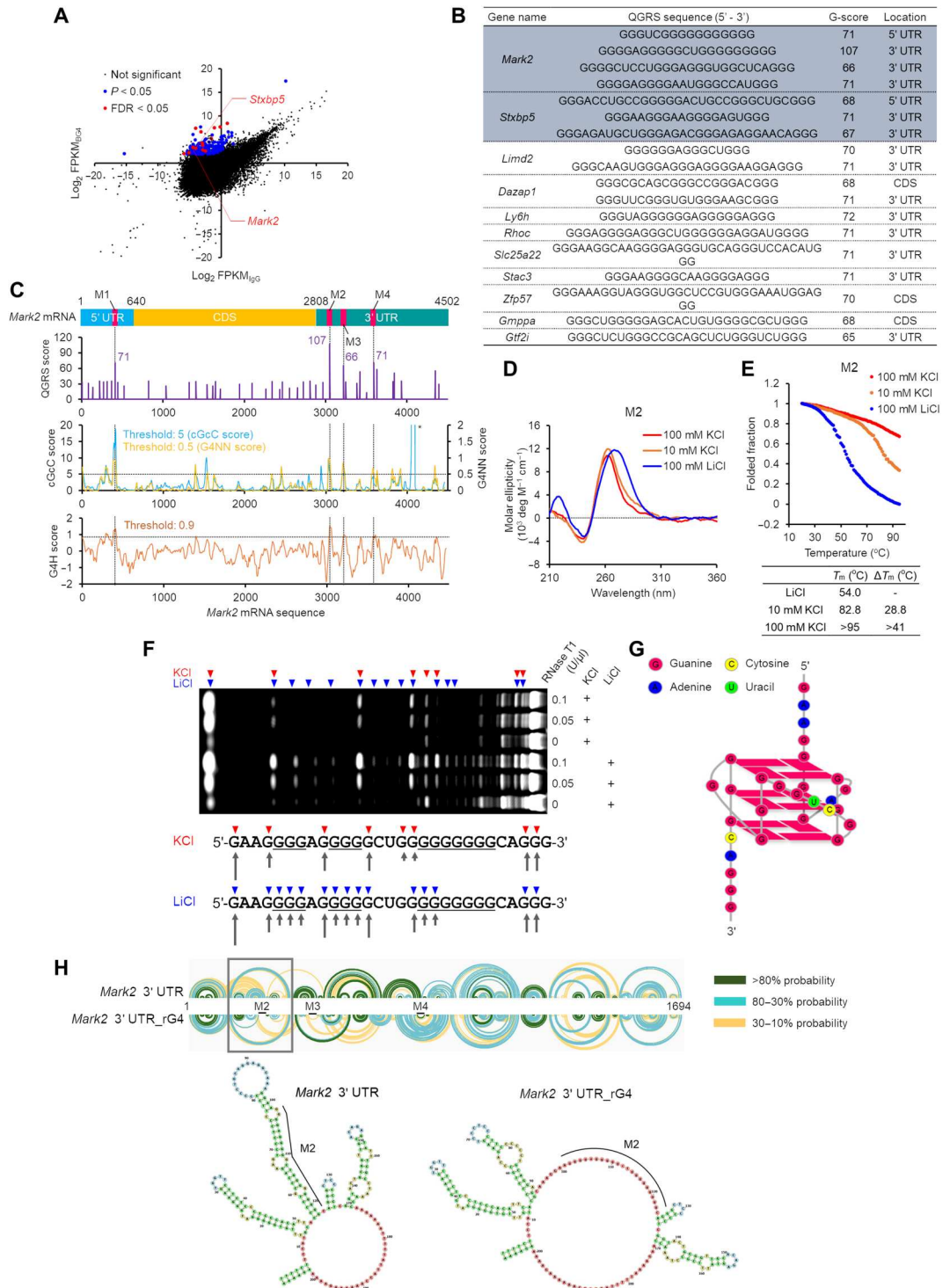
Conversely, the CD spectrum of M3 under 100 mM KCl condition showed a negative band at 210 nm, a feature of A-form hairpin conformation (fig. S8A). The thermal denaturing assay showed a moderate stabilization effect by K+ cations ($\Delta T_m = 6.3$°C), implying a mixture of the A-form hairpin and G4 structure in M3 (fig. S8B). The RNase T1 footprinting assays of M3 under 100 mM KCl and LiCl conditions revealed that guanine residues on a stem-loop region of the predicted A-form hairpin structure were substantially cleaved, whereas they were not cleaved under 100 mM KCl. Instead, pronounced cleavages of loop guanines of predicted G4 structure were detected only under 100 mM KCl (fig. S8, C and D). These results suggested that M3 adopts both conformations, but preferentially forms G4 structures in the presence of K+ cations (fig. S8D). We also characterized the G4 structures of S1, S2, and S3 and revealed that two of the three putative rG4-forming sequences could fold into rigid G4 structures (fig. S9).

On the basis of these biophysical data, we predicted the RNA secondary structure of *Mark2* or *Stxbp5* mRNAs using the

Fig. 2. Comprehensive analysis of rG4-forming mRNAs in mouse brain tissue. (**A**) Scatterplots of BG4-enriched RNAs versus control RNAs (IgG). Dot plots with P values < 0.05 or false discovery rate (FDR) < 0.05 are colored in blue or red, respectively. (**B**) List of the top 11 mRNAs having putative rG4-forming sequences with three G-tetrads (fig. S5A), predicted by the QGRS mapper. (**C**) Visualization of G4 distribution throughout *Mark2* mRNA, which was predicted by several different algorithms: QGRS mapper (top), cGcC (middle), G4NN (middle), and G4H (bottom). The asterisk (*) indicates a polyadenine/uridine region that does not contain any cytosines. This region is overestimated by the cGcC algorithm regardless of the guanine composition. (**D**) CD spectra of M2 (5′-GAAGGGGA GGGGGCUGGGGGGGGGGCAGGG-3′) under KCl or LiCl conditions. (**E**) Thermal denaturing profiles of M2 under KCl or LiCl conditions detected by monitoring CD signals at 260 nm. The values of T_m and differences in T_m values relative to those under LiCl conditions (ΔT_m) are listed. (**F**) RNase T1 footprinting assays of M2 under KCl or LiCl conditions. Arrowheads point to cleavage sites and nucleotides. The length of the arrow represents the extent of cleavage. Underlined guanines can participate in G-tetrads. (**G**) Differential cleavage profiles of M2 between KCl and LiCl conditions, together with CD analyses, determined a three-dimensional structure of M2. (**H**) Schematic for the base-pair probability of the *Mark2* 3′UTR RNA, calculated using a "partition" algorithm provided with the RNAstructure package. The G4 structures identified were reflected by imposing single-stranded constraints on the rG4-forming sequences: *Mark2* 3′UTR_rG4. The arcs represent the connection of base pairs, and the colors represent probability. Secondary structures of the representative part of the *Mark2* 3′ UTR mRNA with or without the constraints are shown below (143 to 348 nucleotides).

Gene name	QGRS sequence (5' - 3')	G-score	Location
Mark2	GGGUCGGGGGGGGGGGG	71	5' UTR
	GGGGAGGGGGCUGGGGGGGGG	107	3' UTR
	GGGGCUCCUGGGAGGGGUGGCUCAGGG	66	3' UTR
	GGGGAGGGGAAUGGGCCAUGGG	71	3' UTR
Stxbp5	GGGACCUGCCGGGGGACUGCCGGGCUGCGGG	68	5' UTR
	GGGAAGGGAAGGGGAGUGGG	71	3' UTR
	GGGAGAUGCUGGGGAGACGGGAGAGGAACAGGG	67	3' UTR
Limd2	GGGGGGGAGGGCUGGG	70	3' UTR
	GGGCAAGUGGGAGGGAGGGGAAGGAGGG	71	3' UTR
Dazap1	GGGCGCAGCGGGCCGGGACGGG	68	CDS
Ly6h	GGGUUCGGGGUGUGGGAAGCGGG	71	3' UTR
Rhoc	GGGAGGGGAGGGCUGGGGGGGAGGAUGGGG	71	3' UTR
Slc25a22	GGGAAGGCAAGGGGAGGGGUGCAGGGUCCACAUGGG	71	3' UTR
Stac3	GGGAAGGGGCAAGGGGAGGG	71	3' UTR
Zfp57	GGGAAAAGGUAGGGUGGCUCCGUGGGGAAAUGGAGGG	70	CDS
Gmppa	GGGCUGGGGGGAGCACUGUGUGGGGCGCUGGG	68	CDS
Gtf2i	GGGCUCUGGGCCGCAGCUCUGGGGUCUGGG	65	3' UTR

RNAstructure package (*37*). For calculation, the G4 structures identified were reflected by imposing single-stranded constraints on the rG4-forming sequences. We found that the G4 formation induced widespread changes in the secondary structures of both *Mark2* and *Stxbp5* mRNA (Fig. 2H and fig. S10).

Binding of DNAPTP6 with rG4-forming mRNAs in vitro and in cells

Next, we examined whether DNAPTP6 directly interacts with these rG4-forming mRNAs using an EMSA. As expected, purified DNAPTP6 protein preferentially bound *Mark2* and *Stxbp5* rG4s compared to non-rG4s (Fig. 3, A to E, and fig. S11). As the band showing the DNAPTP6-RNA complex was not fully detected on
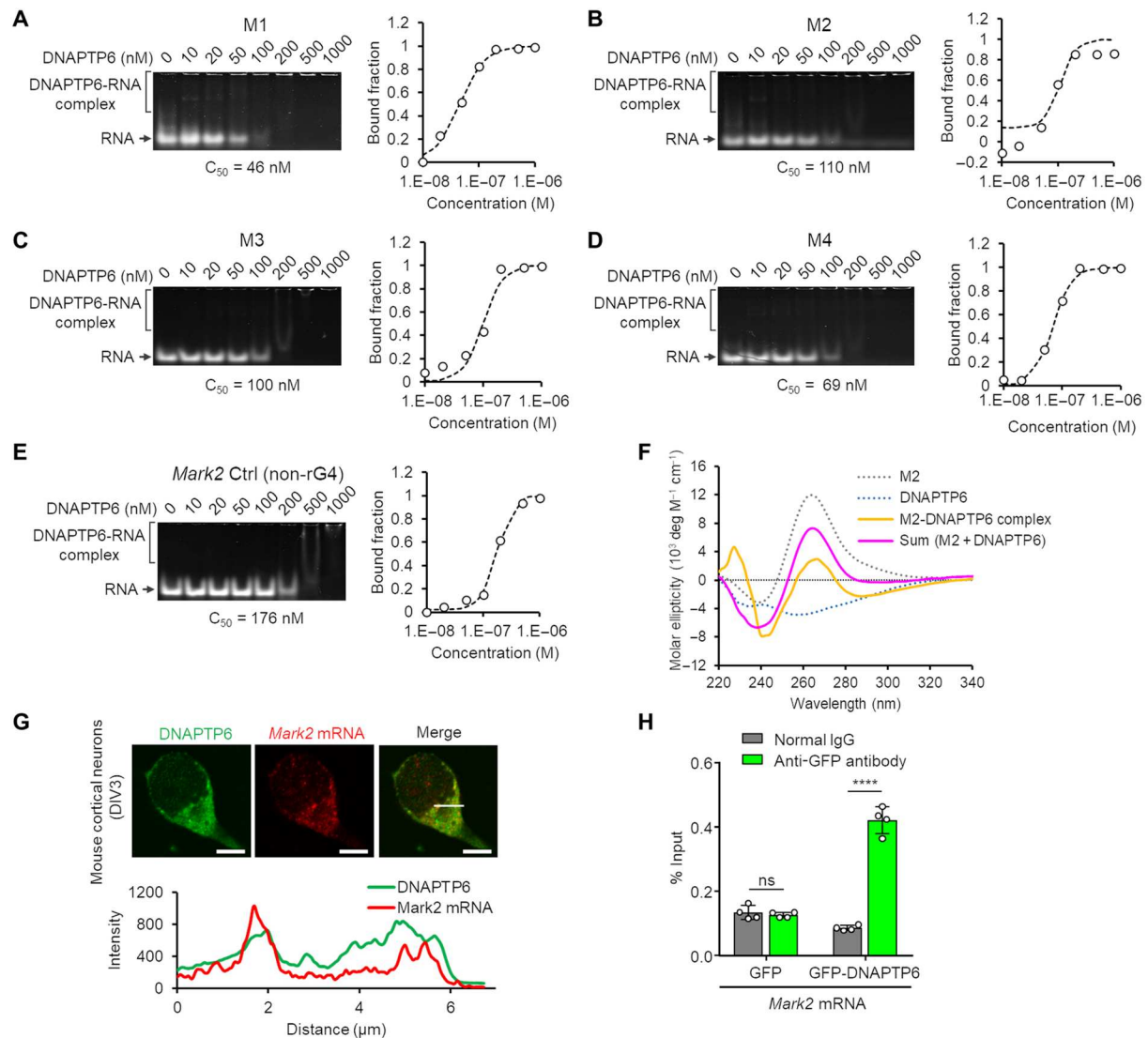
Fig. 3. DNAPTP6 can interact with *Mark2* mRNA in vitro and in cells. (**A** to **D**) EMSA for the interaction of recombinant DNAPTP6 with FAM-labeled *Mark2* RNA oligomers under 100 mM KCl conditions; M1 (5′-CGGGGGUCGGGGGGGGGGGGUGCGG-3′) (A), M2 (B), M3 (5′-UGUGGGGCUCCUGGGAGGGUGGCUCAGGG-3′) (C), M4 (-5′-AGAGGGGAGGGGAAUGGGCCAUGGG-3′) (D), and *Mark2* Ctrl (non-rG4, 5′-CACCUUUCCUCCCUGCCCCAUUG-3′) (**E**). (**F**) CD spectra of M2 only, DNAPTP6 only, and M2 with DNAPTP6. The sum of the respective spectra of M2 only and DNAPTP6 only is also represented. (**G**) Representative confocal images of endogenous DNAPTP6 and *Mark2* mRNA in a mouse cortical neuron (DIV3). DNAPTP6 is substantially colocalized with *Mark2* mRNA. Scale bars, 5 μm. (**H**) RIP-qPCR by anti-GFP antibody using Neuro-2A cells transiently expressing GFP-tagged DNAPTP6 or GFP (mock). ****$P < 0.0001$ (two-sided, unpaired Student's *t* test); $n = 4$ samples from two independent experiments. Error bars represent SD.

the gel because of its large molecular size, half-maximum binding concentration (C_{50}) calculated from the gel band showing only RNA was used for quantification. We confirmed that DNAPTP6 exhibited submicromolar binding affinities to *Mark2* and *Stxbp5* rG4s. The physical interaction between DNAPTP6 and *Mark2* rG4 was further confirmed by CD spectroscopic analysis; the addition of purified DNAPTP6 protein revealed substantial changes in the CD spectrum of M2 (Fig. 3F). To obtain an insight into the interaction of endogenous DNAPTP6 with *Mark2* mRNA, we performed in situ hybridization together with immunostaining in mouse cortical neurons. We observed high colocalization between DNAPTP6 and *Mark2* mRNA in the cytoplasm (Pearson's rank correlation coefficient of 0.61) (Fig. 3G). Experiments using the

cells expressing the deletion mutants showed that expressed GFP-ΔIDR1 was more likely colocalized with *Mark2* and *Stxbp5* mRNAs compared with GFP-ΔCCD and GFP-ΔIDR2, suggesting a prime role of CCD and IDR2 in interacting with *Mark2* and *Stxbp5* mRNAs (fig. S12). RNA immunoprecipitation coupled with quantitative polymerase chain reaction (RIP-qPCR) also validated the in-cell interaction of DNAPTP6 with *Mark2* mRNA in cells expressing GFP-FL (Fig. 3H).

Boosting DNAPTP6 phase separation by self-assembly of rG4s

Proteins with large IDRs such as prion-like domains and low complexity domains can drive protein LLPS and reversibly form

intracellular membrane-less droplets, including SGs (*38*). As expected, purified full-length DNAPTP6 protein formed spherical phase-separating droplets under physiological conditions in vitro, which were attenuated by adding a hydrophobic disruptor, 1,6-hexanediol (Fig. 4A). Phase separation of DNAPTP6 was dependent on protein concentration and inversely proportional to sodium ion concentration (fig. S13A), and DNAPTP6 droplets can fuse with each other (fig. S13B). In fluorescence recovery after

photobleaching (FRAP) assays, the fluorescence from fluorescein-labeled DNAPTP6 droplets was rapidly recovered after photobleaching (Fig. 4B). These results indicated that DNAPTP6 can undergo LLPS. Further analysis for recombinant proteins of each domain of DNAPTP6 revealed that the phase-separating property is derived from IDR1 and IDR2 (fig. S13C). DNAPTP6 droplets grew with the addition of rG4 oligomers (TERRA) but not with non-rG4 oligomers (mTERRA) (Fig. 4A), and the dynamic nature
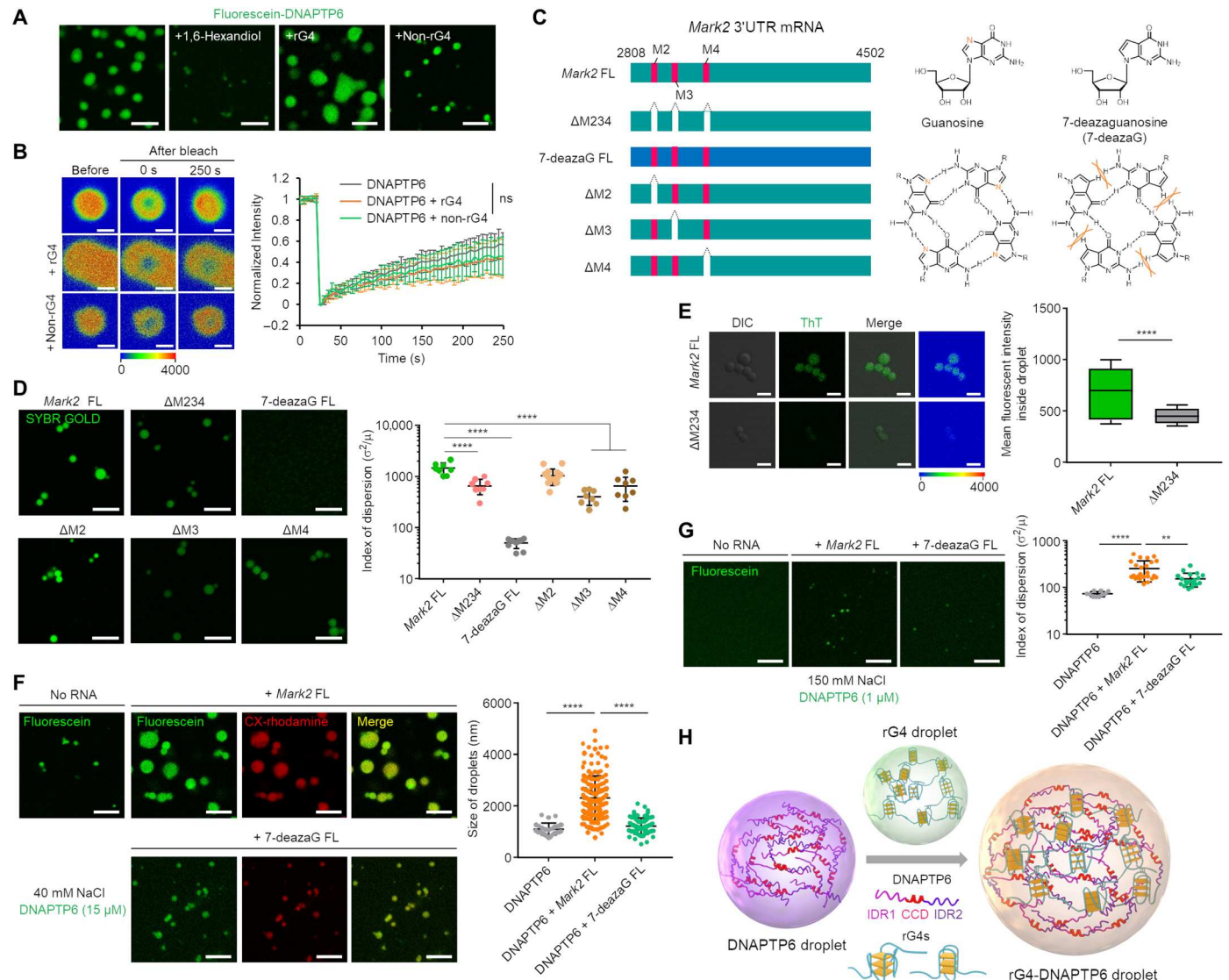

Fig. 4. Self-assembly of rG4s boosts DNAPTP6 phase separation. (**A**) Fluorescence images of droplets formed by 29 μM nonlabeled and 1 μM fluorescein-labeled DNAPTP6 with or without 1,6-hexanediol, rG4 oligomer (TERRA), or non-rG4 oligomer (mTERRA) treatment. Scale bars, 5 μm. (**B**) FRAP assays of droplets formed by DNAPTP6, DNAPTP6 + rG4, and DNAPTP6 + non-rG4. Scale bars, 1 μm. $n = 4$ droplets. (**C**) Schematic for *Mark2* 3′UTR mRNA and its mutants. 7-Deazaguanosine substitution can impair G-tetrad formation. (**D**) Fluorescence images of droplets formed by *Mark2* 3′UTR mRNA and its mutants, detected with SYBR Gold. Scale bars, 5 μm. ****$P < 0.0001$; $n = 7$ to 11 imaging areas. (**E**) Fluorescence images of droplets formed by *Mark2* FL and ΔM234, detected with 3 μM ThT. Scale bars, 2 μm. ****$P < 0.0001$; $n = 22$ (*Mark2* FL) and 12 (ΔM234) droplets. (**F**) Fluorescence images of droplets formed by 14 μM nonlabeled and 1 μM fluorescein-labeled DNAPTP6 with or without CX-rhodamine–labeled *Mark2* FL and 7-deazaG FL. Scale bars, 5 μm. ****$P < 0.0001$; $n = 25$ (DNAPTP6), 158 (DNAPTP6 + *Mark2* FL), and 74 (DNAPTP6 + 7-deazaG FL) droplets. (**G**) Fluorescence images of droplets formed by 1 μM fluorescein-labeled DNAPTP6 proteins with or without *Mark2* FL or 7-deazaG FL. Scale bars, 5 μm. **$P < 0.01$, ****$P < 0.0001$; $n = 10$ (DNAPTP6), 24 (DNAPTP6 + *Mark2* FL), and 21 (DNAPTP6 + 7-deazaG FL) imaging areas. (**H**) Schematic for rG4-associated phase separation. All quantification was done from two independent experiments. Statistical significance was tested by one-way ANOVA Bonferroni's multiple comparison test (B, D, F, and G) or two-sided, unpaired Student's *t* test (E). Error bars represent SD. Boxes in (E) range from lower to upper quartiles with line at median; whiskers show range of data.
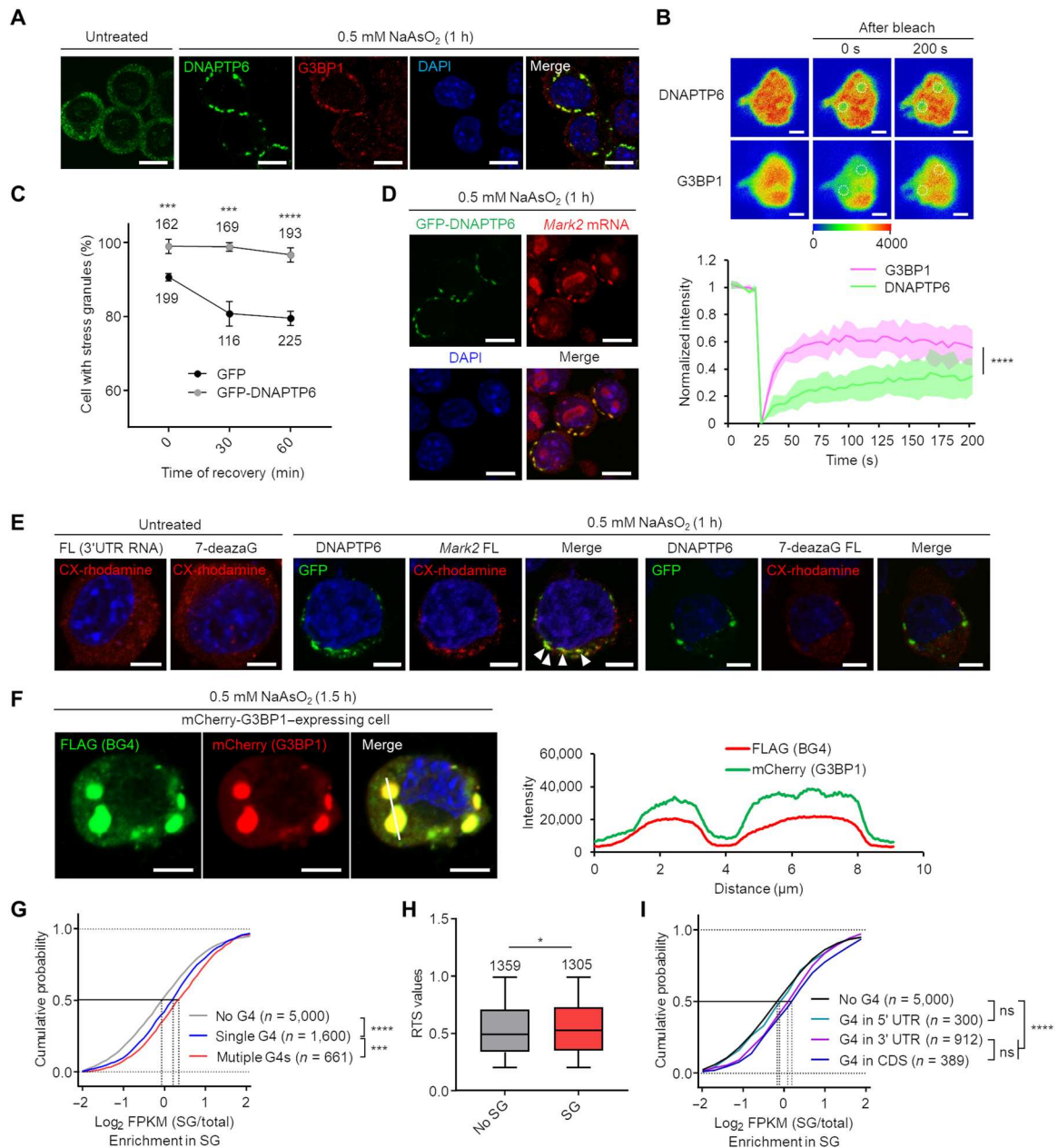
Fig. 5. rG4-associated phase separation contributes to SG organization. (**A**) Representative confocal images of Neuro-2A cells treated with NaAsO$_2$ using anti-DNAPTP6 and anti-G3BP1 antibodies. Scale bars, 10 μm. (**B**) In-cell FRAP assays of DNAPTP6- and G3BP1-positive SGs. Scale bars, 1 μm. ****$P < 0.0001$ (two-way ANOVA with Bonferroni's multiple comparison test); $n = 6$ measurements from three independent experiments. (**C**) Ratio of cells recovered from G3BP1-positive SGs after the depletion of NaAsO$_2$ in Neuro-2A cells transiently expressing GFP or GFP-FL. The percentage of cells with SGs was calculated from three independent experiments. The number of total counted cells for each time point is indicated in the graph. ***$P < 0.001$ and ****$P < 0.0001$ (two-way ANOVA with Bonferroni's multiple comparison test). (**D**) In situ hybridization and immunostaining of Neuro-2A cells transiently expressing GFP-FL with NaAsO$_2$ treatment for detecting DNAPTP6 and endogenous *Mark2* mRNA. Scale bars, 10 μm. (**E**) Representative fluorescence images of Neuro-2A cells transiently expressing GFP-FL, which was transfected with *Mark2* FL or 7-deazaG FL labeled with CX-rhodamine 6 hours before cell fixation with or without NaAsO$_2$ treatment. Scale bars, 5 μm. (**F**) Representative confocal images of Neuro-2A cell transiently expressing mCherry-G3BP1 with NaAsO$_2$ treatment. G4 was visualized with BG4 and anti-FLAG. Scale bars, 5 μm. (**G**) Cumulative distribution of mRNA enrichment in SGs for mRNAs classified by the number of rG4-forming sequences per transcript. ***$P < 0.001$ and ****$P < 0.0001$ (Kolmogorov-Smirnov test). (**H**) Comparison of reverse transcription stop (RTS) values between SG-depleted and SG-enriched rG4s. *$P < 0.05$ (two-sided, unpaired Student's t test). (**I**) Cumulative distribution of mRNA enrichment in SGs for mRNAs classified by the location of rG4-forming sequences. ****$P < 0.0001$ (Kolmogorov-Smirnov test). Error bars represent SD. Boxes in (H) range from lower to upper quartiles with line at median; whiskers show range of data.

of DNAPTP6 droplets was maintained under all conditions (Fig. 4B), suggesting promoting effects of rG4s on DNAPTP6 phase separation.

An rG4 itself is considered to have the potential to trigger RNA phase separation (39–41). Thus, we investigated whether *Mark2* rG4s exhibit phase-separating potential. We observed that M1, M2, and M4 formed phase-separating condensates on their own (fig. S14A). Particularly, M4 formed larger spherical droplets than the others, and the fluorescence was largely recovered after 230 s, thus indicating the dynamic property inside the droplets (fig. S14, A and B). The droplet formation of M4 relied on Mg^{2+} and RNA concentrations (fig. S14C), suggesting that intermolecular interaction is essential for efficient phase separation of this RNA (40). By contrast, mTERRA and M3, which are predominantly folded into a hairpin form, did not cause any phase-separating condensates (fig. S14A). These findings suggest that the intermolecular interaction of G4 structures serves as phase-separating self-assembly RNAs.

To further explore rG4 phase separation, we synthesized a 1695–base pair (bp) full-length *Mark2* 3′UTR mRNA (*Mark2* FL) by in vitro transcription (Fig. 4C). *Mark2* FL showed phase separation that was similar to that of artificial synthetic oligomers (Fig. 4D). Furthermore, the deletion mutant mRNAs (ΔM234), which lack rG4-forming sequences, significantly weakened the formation of droplets (Fig. 4D). To precisely evaluate the need for the structure of rG4s, we also prepared a *Mark2* FL counterpart in which guanosines were fully substituted with 7-deazaguanosines (7-deazaG FL). 7-Deazaguanosine substitution can impair G4 formation without influencing Watson-Crick base pairing capability (Fig. 4C) (42). 7-deazaG FL completely inhibited the droplet formation (Fig. 4D), indicating that G4 structures are essential for RNA self-assembly in *Mark2* FL. We confirmed that *Mark2* FL inside the droplets adopted G4 structures compared with ΔM234, as evidenced with the G4-specific fluorescent dyes thioflavin T (ThT) (Fig. 4E) (43) and *N*-methyl mesoporphyrin IX (NMM) (fig. S15) (44). These findings indicated that the rG4-forming capabilities, rather than the sequences themselves, play a substantial role in RNA phase separation.

Next, we investigated whether rG4-forming mRNAs influence DNAPTP6 phase separation. We found that *Mark2* FL significantly increased the size of the DNAPTP6 droplets, thereby promoting DNAPTP6 phase separation (Fig. 4F). This promotion of DNAPTP6 phase separation was not observed in the case of 7-deazaG FL (Fig. 4F). Moreover, G4 structures can catalyze the formation of DNAPTP6 droplets; the DNAPTP6 solution with a low concentration (1 μM) under 150 mM NaCl remained almost in aqueous form (fig. S13A), whereas the addition of *Mark2* FL significantly induced the formation of DNAPTP6 droplets compared with the addition of 7-deazaG FL (Fig. 4G). Cumulatively, these findings indicate that the phase-separating ability of rG4s serves to boost the droplet formation driven by DNAPTP6 phase separation (Fig. 4H).

Contribution of rG4-associated phase separation to SG organization

To explore the phase-separating property of DNAPTP6 in cells, we focused on SGs, cytoplasmic membrane-less compartments driven by LLPS, as DNAPTP6 was known to be an SG component in mammalian cell lines (33, 45). Treatment of Neuro-2A cells with sodium arsenite ($NaAsO_2$) confirmed that DNAPTP6 localized with SGs positive for G3BP1, a commonly used SG marker (Fig. 5A). Next, we coexpressed GFP-FL and mCherry-tagged G3BP1 (mCherry-G3BP1) in Neuro-2A cells and measured the dynamics of these proteins in $NaAsO_2$-induced SGs using FRAP. Although mCherry-G3BP1 fluorescence was largely recovered within 100 s, GFP-FL fluorescence was not fully recovered (Fig. 5B). To eliminate artifacts from overexpressed GFP-tagged DNAPTP6, we tagged endogenous DNAPTP6 with mNeonGreen via the CRISPR-Cas9 system. We confirmed that endogenous DNAPTP6 was recruited into SGs and had a high motility inside SGs (fig. S16). We next asked whether DNAPTP6 was involved in the formation and/or maintenance of SG (45). Expression of GFP-FL significantly retained mCherry-G3BP1−positive SGs after the depletion of $NaAsO_2$ compared to that of GFP (Fig. 5C), suggesting that DNAPTP6 plays a role in the maintenance for SGs. In addition, GFP-ΔCCD and GFP-ΔIDR2 were less colocalized with G3BP1-positive SGs and showed diffused localization compared with GFP-FL and GFP-ΔIDR1 (fig. S17A), indicating that CCD and IDR2 are critical for DNAPTP6 participating in SGs.

As we have figured out the phase-separating property of DNAPTP6 to maintain SGs, we next test whether organizing SGs is mediated by rG4s. We first observed the cellular behavior of *Mark2* mRNA under $NaAsO_2$-stressed condition. In $NaAsO_2$-stressed cells, the accumulation of endogenous *Mark2* mRNAs into SGs was observed, as evidenced by colocalization with DNAPTP6 (Fig. 5D). To evaluate the role of G4 structures within *Mark2* mRNA on recruitment into SGs, CX-rhodamine−labeled *Mark2* FL and 7-deazaG FL were transfected into cells. In unstressed cells, transfected *Mark2* FL and 7-deazaG FL were evenly distributed throughout the cytoplasm (Fig. 5E). In contrast, in $NaAsO_2$-stressed cells, *Mark2* FL was colocalized with DNAPTP6-positive SGs, but 7-deazaG FL was not (Fig. 5E). These results suggest that rG4s are required for efficient recruitment of *Mark2* mRNAs into DNAPTP6-positive SGs. To further validate the role of rG4s in recruiting mRNAs into SGs, we investigated $NaAsO_2$-induced SG formation in Neuro-2A cells expressing mCherry-G3BP1 and found that BG4 signals accumulated within G3BP1-positive SGs (Fig. 5F).

To support these experimental data, we assessed whether there is a correlation between mRNA enrichment in SGs and rG4s by using data sources from the comprehensive analysis of rG4 and SG transcriptomes (11, 46). The comparison revealed that mRNAs containing a single rG4-forming sequence are more enriched in SGs than non-rG4 mRNAs (Fig. 5G). mRNAs containing multiple rG4-forming sequences are more significantly enriched in SGs compared with those containing a single rG4-forming sequence, regardless of the length of the transcripts (Fig. 5G and fig. S17, B and C). Considering that rG4s enriched in SGs tend to be more stable (Fig. 5H), G4 structures themselves appear to mark mRNAs to be recruited to SGs and regulate the SG transcriptome. Furthermore, we found that the location of G4 structures in mRNAs influenced the SG enrichment of the mRNAs; the mRNA that contained G4 structures at the CDS and the 3′UTR, not the 5′UTR, were significantly enriched in SGs (Fig. 5I). Together with our finding that RNA self-assembly driven by G4 structures promotes DNAPTP6 phase separation, these results suggest that rG4-associated phase separation organizes SG assembly through DNAPTP6.

Neuronal dysfunction induced by impaired rG4-associated SG assembly

Last, to explore the phenotypic impact of rG4-associated SG organization by DNAPTP6 on neurons, we down-regulated the expression of DNAPTP6 via RNA interference using short hairpin RNA (shRNA; shDNAPTP6) and assessed the neuronal function using mouse cortical neurons. We validated that DNAPTP6 expression declined by 45% in mouse cortical neurons using shDNAPTP6 compared with negative control (shCtrl) (fig. S18A). DNAPTP6 down-regulation did not show marked cell death, as assessed by immunoreactivity for cleaved caspase-3 (an apoptosis marker) (fig.

S18B). In addition, endogenous DNAPTP6 was recruited into SGs in neurons following $NaAsO_2$ treatment (fig. S18C). In electrophysiological experiments, we measured the effect of DNAPTP6 knockdown in $NaAsO_2$-stressed neurons on spontaneous excitatory postsynaptic currents (sEPSCs) using whole-cell patch-clamp recordings (Fig. 6A). In shCtrl neurons, $NaAsO_2$ treatment caused a significant decrease of sEPSC amplitude and frequency compared with vehicle-treated (nonstress) condition (Fig. 6B). DNAPTP6–down-regulated neurons exhibited a significant decrease of sEPSC frequency compared with shCtrl neurons under $NaAsO_2$-stressed condition, but no significant differences under nonstress condition
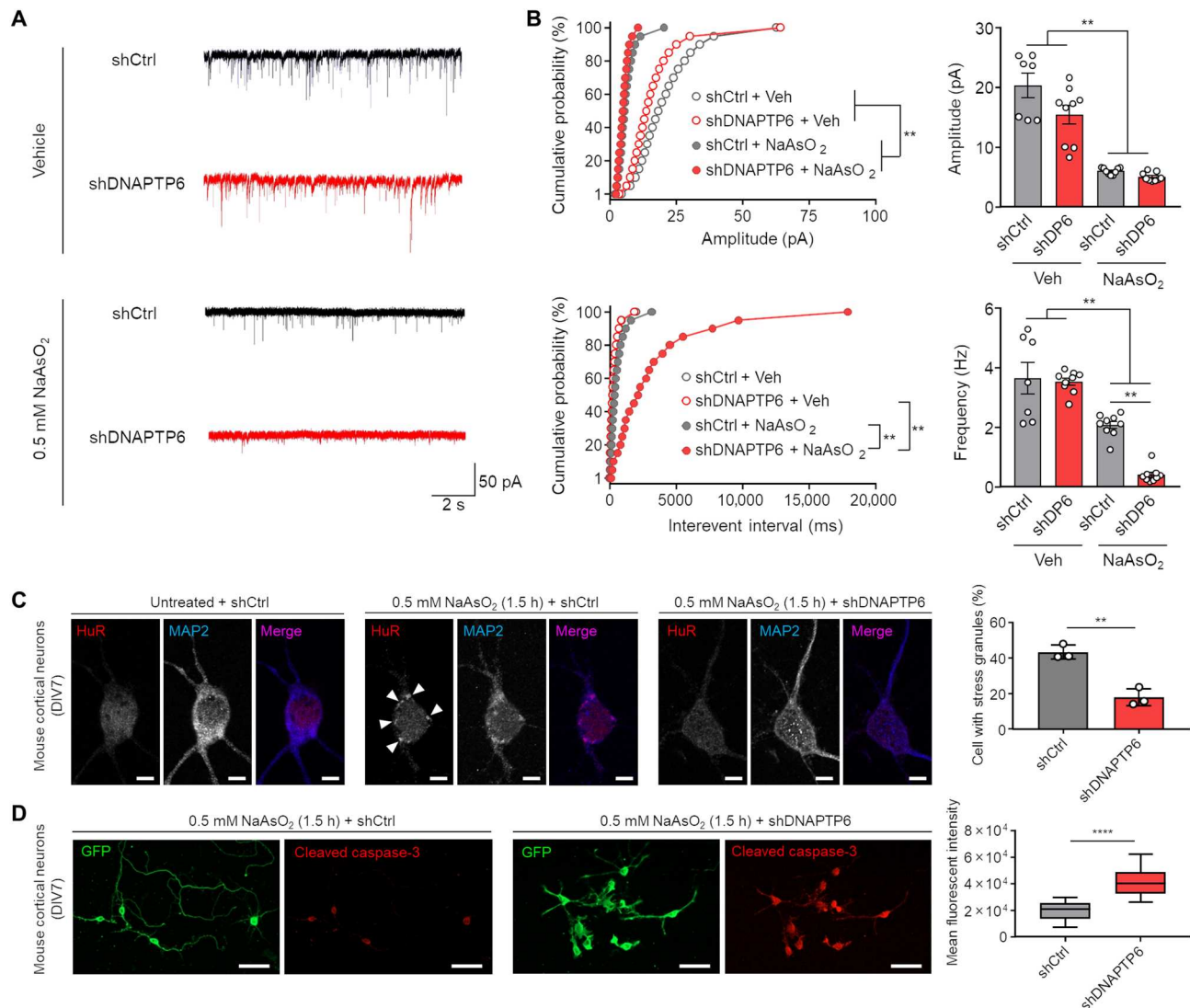

Fig. 6. Impaired rG4-associated SG assembly induces neuronal dysfunction. (**A**) Measurements of sEPSCs using shRNA-expressing mouse cortical neurons (DIV14) with or without $NaAsO_2$ treatment. (**B**) Analysis of amplitude (top) and frequency (bottom) from sEPSCs. n = 7 to 9 cells from two independent experiments. **$P < 0.01$ [two-way (left) or one-way (right) ANOVA with Bonferroni's multiple comparison test]. shDP6: shDNAPTP6. (**C**) Representative confocal images of shRNA-expressing mouse cortical neurons (DIV7) treated with $NaAsO_2$. HuR and MAP2 were visualized as the SG and neuronal markers, respectively. Quantification was conducted from 66 neurons positive for MAP2 and cotransfected GFP in three independent experiments. Arrowheads point to SGs. Scale bars, 5 μm. **$P < 0.01$ (two-sided, unpaired Student's t test). (**D**) Representative confocal images of shRNA-expressing mouse cortical neurons (DIV7) treated with $NaAsO_2$. Cleaved caspase-3 was visualized as a marker for the activation of the apoptotic pathway. A GFP-expressing plasmid was cotransfected to probe shRNA-expressing neurons. Quantification was conducted with 50 neurons positive for cotransfected GFP in two independent experiments. Scale bars, 50 μm. ****$P < 0.0001$ (two-sided, unpaired Student's t test). Error bars in (B) or (C) represent SEM or SD, respectively. Boxes in (D) range from lower to upper quartiles with line at median; whiskers show range of data.

(Fig. 6B). Furthermore, we found that DNAPTP6 knockdown significantly reduced the number of SGs following $NaAsO_2$ treatment (Fig. 6C). Consistent with the electrophysiological results, DNAPTP6–down-regulated neurons showed significantly increased levels of cleaved caspase-3 immunoreactivity compared with shCtrl neurons under $NaAsO_2$-stressed condition (Fig. 6D). Down-regulation of G3BP1, a major and functional SG component, recapitulated phenotypic changes induced by DNAPTP6 knockdown (fig. S19).

To examine which domain of DNAPTP6 is responsible for the SG-associated phenotype, we expressed GFP-FL, GFP-ΔIDR1, GFP-ΔCCD, and GFP-ΔIDR2 in DNAPTP6–down-regulated neurons under $NaAsO_2$-stressed condition. Expression of GFP-FL and GFP-ΔIDR1 restored the decreased sEPSC frequency, reduced the number of SGs, and increased cleaved caspase-3 immunoreactivity, but GFP-ΔCCD and GFP-ΔIDR2 did not (fig. S20). These data support our idea that rG4-associated phase separation derived from CCD and IDR2 domains of DNAPTP6 are required for proper SG organization. Together, these findings suggest that neurons in which rG4-associated SG assembly are impaired became sensitized to oxidative stress, thus causing neuronal dysfunction.

DISCUSSION

In this research, we demonstrate that an rG4BP, DNAPTP6, undergoes phase separation, which is specifically enhanced by G4 structures in vitro and in cells. In neurons, the cellular phase-separating DNAPTP6/rG4 complexes organize SG that is required to maintain neuronal function under oxidative stress condition. Our findings provide insight into the mechanism underlying SG biology for neuronal homeostasis.

We performed a comprehensive analysis of rG4BPs and rG4-containing mRNAs expressed in mouse forebrain (Figs. 1 and 2). We newly identified DNAPTP6 as an rG4BP with high rG4 selectivity and characterized *Mark2* and *Stxbp5* mRNAs as mRNAs containing multiple G4 structures. In vitro, DNAPTP6 directly interacts with *Mark2* and *Stxbp5* mRNAs through G4 structures (Fig. 3). In cells, DNAPTP6 is recruited into SGs with rG4-containing mRNAs to physically maintain SGs (Fig. 5). Down-regulation of DNAPTP6 partially impaired SG formation and displayed neuronal dysfunction under oxidative stress condition, including synaptic transmission defects and neuronal cell death (Fig. 6). This neuronal dysfunction caused by the DNAPTP6 down-regulation was similar to that caused by down-regulation of G3BP1, a prime SG regulator (fig. S19). As G3BP1 was recently reported to be an rG4BP (*47*), rG4-dependent molecular mechanism is involved in neuronal SG biology.

Using a reconstituted system, we could consider the molecular mechanism underlying SG assembly critical for neuronal function (Fig. 4). We found that recombinant DNAPTP6 formed dynamic self-assembly droplets through two IDRs. Synthetic *Mark2* 3′UTR mRNAs also formed liquid-like droplets using G4 structures as scaffolds. The phase-separating capability of rG4s enhances DNAPTP6 phase separation. The fine tuning of DNAPTP6 assembly via rG4 phase separation may contribute to organizing functional SG assembly in neurons.

The mechanism in SG assembly initiation at the 5′UTR is relatively well understood; the phosphorylation of eIF2α inhibits the binding of translation initiation complex, and the incomplete pre-initiation complex contributes to the recruitment of SG components (*48*). However, what occurs in the 3′UTR and CDS and how this contributes to the initiation of SG assembly after polysome detachment have not been fully elucidated. Our data suggest a cis-regulatory role of rG4s at the 3′UTR and CDS of mRNAs upon SG nucleation and assembly, in which the rG4s likely serve as structural basis to assemble rG4BPs and properly augment cellular RNA granule formation. Furthermore, we reveal that the presence of rG4s enhances the partitioning into SGs (Fig. 5, G to I) and influences the entire RNA secondary structure (Fig. 2H and fig. S10). rG4s may be critical factors to regulate mRNA composition and coordinate proper SG transcriptomes.

rG4BPs behave as trans-acting factors for translation and localization of rG4-forming mRNAs. For example, eIF4A recognizes and unfolds G4 structures at the 5′UTR of mRNAs, leading to translational initiation (*49*). Similarly, hnRNAP A2/B1 unwinds G4s, thereby enhancing translational activity probably by promoting ribosome scanning at the 5′UTR (*50*). FMRP, an rG4BP associated with fragile X syndrome, likely recognizes rG4s at the 5′UTR or the 3′UTR of several mRNAs and engages in translational repression or activity-dependent localization of mRNAs (*51*, *52*). These rG4BPs have the propensity to assemble into RNA granules in common, and their mutations and the abnormality of the phase-separating property are often associated with neuronal diseases (*41*, *53*, *54*). rG4-dependent neuronal dysfunction caused by reduced expression of DNAPTP6 likely depends on stress stimuli, considering that expression patterns of *Mark2*, *Stxbp5* mRNAs, and rG4s were not markedly altered upon DNAPTP6 knockdown in unstressed neurons (fig. S21). Although the neuropathogenic features of DNAPTP6 in human SG-associated diseases have not been reported to date, DNAPTP6 may play a requisite role in managing stress stimuli through proper RNA granule formation to prevent pathological consequences in the central nervous system (*48*).

In conclusion, this work provides a previously unknown insight into the physiological roles of rG4s in neurons and mechanistic advances in SG biology, in a way that mediates the rG4-associated phase separation. Considering recent perspectives for potential roles of rG4s in RNA granules (*41*, *55*, *56*), rG4-dependent phase separation may have the more global impact on cellular physiological homeostasis.

MATERIALS AND METHODS
Animals
C57BL/6J mice purchased from Japan SLC Inc. were used for all experiments. Mice were housed under climate-controlled conditions in a 12-hour light/12-hour dark cycle and were provided with standard food and water ad libitum. Animal studies were conducted in accordance with the institutional guidelines of Kumamoto University, Kumamoto, Japan. Ethical approval was obtained from the Animal Care and Use Committee of Kumamoto University.

Reagents
The DNA primers and RNA oligomers used here were purchased from Hokkaido System Science Co. Ltd. $NaAsO_2$ was purchased from Sigma-Aldrich. 1,6-Hexanediol was purchased from Nacalai Tesque. SYBR Gold (SYBR Gold Nucleic Acid Gel Stain) was purchased from Thermo Fisher Scientific. NMM was purchased from

Santa Cruz Biotechnology. ThT was purchased from AnaSpec Inc. Isopropyl-β-D-thiogalactopyranoside (IPTG) was purchased from Protein Ark. 4′,6-Diamidino-2-phenylindole (DAPI; NucBlue Fixed Cell ReadyProbes Reagent) was purchased from Thermo Fisher Scientific.

Antibodies
The following primary antibodies were used: anti-GFP (1:500; 632380, Clontech), anti-HuR (1:200; 11910-1-AP, Proteintech), anti-DNAPTP6 (1:300; 16938-1-AP, Proteintech), anti-MAP2 (1:1000; ab5392, Abcam), anti-G3BP1 (1:300; 13057-2-AP, Proteintech), recombinant BG4 (anti-G4, manually prepared, used at 1 μg/ml), anti-6×His (1:1000; ab18184, Abcam), anti-TIA1 (1:1000; sc-1751, Santa Cruz Biotechnology), anti-Tuj1 (tubulin β-3) (1:1000; 802001, BioLegend), anti–cleaved caspase-3 (1:200; ab2302, Abcam), anti-DYKDDDDK tag (1:800; 14793S, Cell Signaling Technology), anti-FLAG (1:1000; F1804, Sigma-Aldrich), anti-FMRP (1:1000; MAB2160, Millipore), and anti-digoxigenin (1:1000; ab76907, Abcam). For immunocytochemistry and immunohistochemistry, the following secondary antibodies were used: Alexa Fluor 488–conjugated donkey anti-rabbit (1:500; A-21206, Thermo Fisher Scientific), Alexa Fluor 594–conjugated donkey anti-rabbit (1:500; A-21207, Thermo Fisher Scientific), Alexa Fluor 488–conjugated donkey anti-mouse (1:500; A-21202, Thermo Fisher Scientific), Alexa Fluor 594–conjugated donkey anti-mouse (1:500; A-21203, Thermo Fisher Scientific), Alexa Fluor 594–conjugated donkey anti-goat (1:500; A-11058, Thermo Fisher Scientific), and DyLight 405–AffiniPure donkey anti-chicken IgY (1:500; 703-475-155, Jackson ImmunoResearch).

Plasmids
The mammalian expression plasmid of GFP-tagged DNAPTP6 (pCAG-GFP-DNAPTP6) was prepared from the pCAG neo vector (Fujifilm) by In-Fusion HD cloning (Takara Bio) using GFP and DNAPTP6 inserts. The DNAPTP6-coding insert was generated from the pFN21A-HaloTag-DNAPTP6 plasmid (Kazusa DNA Research) by standard PCR method. Plasmids for deletion mutants were generated using the KOD-Plus Mutagenesis Kit (Toyobo). The mammalian expression plasmid of mCherry-tagged G3BP1 (pCAG-mCherry-G3BP1) was prepared from the pCAG neo vector (FujiFilm) by In-Fusion HD cloning (Takara Bio) using an mCherry/G3BP1 insert. The G3BP1 insert was adapted from pEGFP-C1-G3BP1-WT (deposited from A. Leung laboratory; Addgene, plasmid no. 135997). The *Escherichia coli* (*E. coli*) expression plasmids of SUMO-tagged DNAPTP6 and deletion mutants were prepared from the pET-SUMO Expression System (Thermo Fisher Scientific). pSANG10-3F-BG4 (deposited from S. Balasubramanian laboratory; Addgene, plasmid no. 55756) was used to prepare recombinant BG4. A series of DNAPTP6 shRNA plasmids were purchased from Sigma-Aldrich (MISSION TRCN0000263403, TRCN0000263404, TRCN0000263405, TRCN0000282603, and TRCN0000282607). After validation of DNAPTP6 knockdown efficiency, we chose to use TRCN0000263405 (shDNAPTP6). G3BP1 shRNA plasmid was purchased from Sigma-Aldrich (MISSION TRCN0000279148). The nontargeting hairpin control, SHC002 (Sigma-Aldrich), which contains a sequence that does not target any known human or mouse gene, was used as a negative control (shCtrl). Plasmids containing *Mark2* 3′UTR complementary DNA (cDNA; pCAG-*Mark2* 3′UTR) were prepared from the pCAG neo vector (Fujifilm) by In-Fusion HD cloning (Takara Bio) using *Mark2* 3′UTR cDNA inserts obtained from Neuro-2A total RNAs. Plasmids for G4 deletion mutants were generated using the KOD-Plus Mutagenesis Kit (Toyobo) from the pCAG-*Mark2* 3′UTR plasmid.

Cell culture
The Neuro-2A mouse neuroblastoma cell line CCL-131 was authenticated by the provider using short tandem repeat profiling (American Type Culture Collection). Neuro-2A cells were routinely cultured on Dulbecco's modified Eagle's medium (Sigma-Aldrich) supplemented with 10% fetal bovine serum (FBS; Gibco) and 1× penicillin/streptomycin (Gibco) at 37°C in a humidified atmosphere of 5% CO_2. HepG2 cells were cultured using the same growth medium. Neuro-2A cells were transfected with protein expression vectors using Lipofectamine 2000 transfection reagents or with mRNAs using TransIT-mRNA transfection reagents (Mirus). Primary culture of the mouse cortical neurons was conducted as described previously (*57*). Briefly, cortical tissue from embryonic day 18 C57BL/6J mice (Japan SLC Inc.) was dissected and dispersed. Cells were seeded on coverslips coated with poly-L-lysine (PLL) in minimum essential medium (Thermo Fisher Scientific) supplemented with 10% FBS, 0.6% glucose (Wako), and 1 mM pyruvate (Sigma-Aldrich). After cell attachment, cells were cultured in neuron culture medium (Wako) at 37°C in a humidified atmosphere of 5% CO_2. Cells were transfected with expression vectors using electroporation on a NEPA21 electroporator (NEPAGENE) at 0 day in vitro (DIV0) and collected at DIV3 or DIV7 for subsequent biochemical experiments.

BG4 RIP-seq
Mouse forebrain tissues were lysed and precleared using the Protein G HP SpinTrap Kit (GE Healthcare). The precleared samples were incubated at 4°C overnight in a Protein G HP SpinTrap column that had been treated with His-tagged BG4 (or normal rabbit IgG for control) and anti-6×His. The resultant solution was washed three times with wash buffer and eluted with elution buffer. Wash buffer and elution buffer were provided with the RiboCluster Profiler RIP-Assay Kit (MBL). The BG4-bound RNA fraction was purified using the RNeasy Mini Kit (Qiagen) and subjected to RNA-sequencing library preparation using the Ion Total RNA-Seq Kit v2 (Thermo Fisher Scientific). The cDNA libraries obtained were sequenced on an Ion Proton sequencer (Thermo Fisher Scientific). Data were processed using the Torrent Suite Software v.5.2.2 (Thermo Fisher Scientific) to remove adapter sequences and low-quality ends. The Cufflinks software package was used to analyze BG4-enriched mRNAs compared with IgG-treated samples. Putative rG4-forming motifs of mRNAs were predicted using the QGRS mapper (http://bioinformatics.ramapo.edu/QGRS/index.php) and QuadBase2 (http://quadbase.igib.res.in/).

Identification of BG4-interacting proteins by LC-MS/MS
Mouse forebrain tissues were lysed in a buffer containing 50 mM tris-HCl (pH 7.5), 0.15 M NaCl, 0.1% Triton X-100, 4 mM EDTA, 4 mM EGTA, 1 mM Na_3VO_4, 50 mM NaF, 1 mM dithiothreitol, and protease inhibitors (trypsin inhibitor, pepstatin A, and leupeptin) and centrifuged at 15,000g for 10 min. Supernatants were collected and incubated at 4°C for 4 hours with constant

rotation on a Protein A Sepharose Column (GE Healthcare) that had been prebound with His-tagged BG4 (or normal rabbit IgG for control) and anti-6×His. The bound proteins were then washed with tris-buffered saline and eluted with 2.5% acetic acid. The solution was exchanged and concentrated with 50 mM triethylammonium bicarbonate using Amicon Ultra-0.5 and then electrophoresed. The protein samples obtained from the gels were reduced and alkylated and then digested with trypsin. LC-MS/MS analysis of all samples was outsourced to Oncomics Co. Ltd. Proteins identified in the control samples that were pulled down with 10 µg of mouse IgG were subtracted from the identified proteins.

Protein expression and purification

SUMO-tagged proteins were expressed in *E. coli* strain Rosetta2 pLysS (DE3) (Novagen) by adding 0.5 mM IPTG and incubating for 20 hours at 16°C. Cells were pelleted and resuspended in 20 mM Hepes-KOH buffer (pH 7.5) containing 500 mM KCl, 1× protein inhibitor cocktail (Nacalai Tesque), and RNase A (0.1 mg/ml; Qiagen). Cell suspensions were sonicated, and the filtered supernatant was subjected to HisPur Cobalt Resin (Thermo Fisher Scientific). The proteins eluted with imidazole solution were further purified in a HiTrap SP HP column in 50 mM Hepes-KOH (pH 7.5) buffer at a flow rate of 1.0 ml/min with a linear gradient elution of 0 to 100% of 1 M NaCl. The fractions were checked by SDS–polyacrylamide gel electrophoresis, and the target fractions were concentrated using an Amicon Ultra-15 or Ultra-4 centrifugal filter unit (Millipore). After dialysis in 20 mM Hepes-KOH (pH 7.5) buffer containing 200 mM NaCl, 10% glycerol, and 3 mM dithiothreitol, purified SUMO-tagged proteins were quantified by the bicinchoninic acid method and stored below −80°C.

Electrophoresis mobility shift assay

Fluorescein phosphoramidite (FAM)–labeled RNAs (20 nM) in 10 mM tris-HCl (pH 7.5) containing 100 mM KCl or LiCl were heated at 95°C and gradually cooled to room temperature over 1.5 hours. A recombinant DNAPTP6 and its mutants with specified concentrations were added to the folded RNA samples and then incubated at room temperature for a minimum of 30 min. The resulting mixtures were analyzed by gel electrophoresis [6% native tris-borate EDTA (TBE) polyacrylamide, 90 min, 100 V, 4°C]. RNAs on the gels were visualized with Typhoon Trio equipment (GE Healthcare). For K_d determination for the interaction of RNA with DNAPTP6 and its mutants, the band shift data were fitted by a nonlinear least square method using the following equation

$$B_{app} = 2^{-1}[RNA]^{-1}\{(K_d + [RNA] + [Protein]) - [(K_d + [RNA] + [Protein]) - 4[RNA][Protein]]^{1/2}\}$$

where B_{app} is the ratio of the intensity of RNA-protein complex bands to the intensity of an RNA band of a lane without proteins; K_d is the dissociation constant; [RNA] is the total RNA concentration; and [Protein] is the total protein concentration.

C_{50} was calculated from fitting by a nonlinear least square method using the following equation

$$Y = A_{min} + \{(A_{max} - A_{min})/[1 + 10^{n(\log 10 C50 - \log 10 C)}]\}$$

where Y is the intensity of a band showing an RNA only in no protein condition subtracted from the intensity of a band

showing an RNA only in each condition of the protein concentration, A_{min} is the minimum intensity of a band showing an RNA only, A_{max} is the maximum intensity of a band showing an RNA only, and C is the total protein concentration in each condition.

SPR-binding assays

SPR experiments were performed on a Biacore X instrument (GE Healthcare) according to a previous report, with some modifications (*58*). Biotinylated RNA was immobilized to streptavidin-functionalized sensor chips to obtain the desired immobilization level (approximately 10 to 14 response units). SPR measurements were performed using degassed and filtered HBS buffer [10 mM Hepes (pH 7.4), 150 mM NaCl, 3 mM EDTA, and 0.005% surfactant P20] with 100 mM KCl at 25°C. A series of sample solutions with a wide range of concentrations were prepared in the same buffer and injected at a flow rate of 50 µl/min. After each cycle, the samples remaining on the RNA were detached with 10 mM glycine (pH 2.0) until the baseline of the sensorgrams was restored. The resulting sensorgrams were fitted with a model for 1:1 Langmuir binding on the BIAevaluation v.4.1 program.

CD spectroscopy

RNA oligomers (2.5 µM) were prepared in 10 mM tris-HCl (pH 7.5) buffer containing KCl (100 and 10 mM) or LiCl (100 mM), and all RNA oligomers were refolded by a heat/cooling process before the experiments were conducted. CD spectra were recorded at 25°C and 200 to 350 nm on a JASCO J-805LST spectrometer in a 3-mm pathlength quartz cuvette. For the RNA denaturing assays, the maximum CD signals of each RNA at 262 nm were monitored. Temperature scans were performed continuously from 25° to 95°C at a rate of 1°C/min. T_m values were determined as the temperature at half of the maximum signal increase.

RNase T1 footprinting

Footprinting experiments were performed according to a previous report, with some modifications (*59*). FAM-labeled RNA oligomers (1.5 µM) were prepared in 10 mM tris-HCl (pH 7.5) buffer containing 100 mM KCl or LiCl, and all RNA oligomers were refolded by a heat/cooling process before the experiments were conducted. RNA was treated with RNase T1 (Thermo Fisher Scientific) at room temperature for 3 min, and then a urea-based buffer was added to terminate the reaction. Aliquots of the resultant solution were loaded onto a 15% TBE–urea polyacrylamide (acrylamide:bis-acrylamide, 19:1) gel and electrophoresed at 1500 V for 2 hours in 1× TBE running buffer. The RNAs on the gels were visualized using Typhoon Trio equipment (GE Healthcare).

Immunocytochemistry and immunohistochemistry

For immunocytochemistry, primary cultured neurons, Neuro-2A cells, and HepG2 cells were fixed with 4% paraformaldehyde (PFA) in 1× phosphate-buffered saline (PBS) and permeabilized with 0.3% Triton X-100 in PBS. Primary cultured neurons were pretreated with cold methanol for 1 min on ice before the Triton X-100 treatment to efficiently permeabilize neurites. After blocking with 3% bovine serum albumin in PBS, cells were incubated with primary antibodies overnight at 4°C and with secondary antibodies for 3 hours at room temperature. Nuclei were stained with DAPI. Samples were mounted on glass slides using VECTASHIELD Mounting Medium (Vector Laboratories). For rG4 staining with

BG4, we used diethyl phosphorocyanidate (DEPC) treated with PBS throughout the process in an RNase-free environment. Fluorescence images were obtained using an LSM780 microscopy system (Carl Zeiss). For immunohistochemistry, brain slices were fixed with 4% PFA in PBS and permeabilized with 0.3% Triton X-100 in PBS.

Live-cell imaging and FRAP assays
Cells were grown on PLL-coated coverslips in 12-well plates for 48 hours and treated with 0.5 mM NaAsO$_2$ 1 to 1.5 hours before measurement. The coverslip was placed in an imaging chamber (Chamlide), and fluorescence images were obtained using the LSM780 microscopy system (Carl Zeiss). Photobleaching was performed with 100% laser power to 50% intensity using the bleaching program in ZEN software. Time-lapse images were recorded every 5 s using a Zeiss Objective Plan-Apochromat 63×/1.4 oil differential interference contrast (DIC) M27 to track photorecovery.

CRISPR-Cas9 knock-in
Knock-in by CRISPR-Cas9 was performed as described previously (60). A single-stranded homology-directed repair DNA template containing 800–nucleotide (nt)–long homology arms flanking an mNeonGreen CDS was designed to be located immediately before the stop codon of DNAPTP6. The donor single-stranded DNA (ssDNA) was prepared using the Long ssDNA Preparation Kit (BioDynamics Laboratory Inc.). Transfection was performed using Lipofectamine CRISPRMAX according to the manufacturer's protocol. The mixture of three single-guide RNAs targeted across the stop codon of DNAPTP6 and a Cas9 protein (HiFi Cas9 Nuclease V3) was used for the efficient double-strand break and knock-in. HepG2 cell lines were used because DNAPTP6 is strongly expressed in this cell lines, thus allowing live-cell imaging and FRAP experiments of endogenous DNAPTP6.

In situ hybridization
For RNA probe preparation, total RNAs were extracted from adult mouse cortex tissues and purified using the RNeasy Mini Kit (Qiagen) according to the manufacturer's instructions. cDNA was obtained via reverse transcription using the PrimeScript RT Reagent Kit with gDNA Eraser (Takara Bio). cDNAs corresponding to *Mark2* and *Stxbp5* mRNA probes were then amplified using the PrimeStar Max DNA Polymerase (Takara Bio) with a standard PCR protocol to obtain 586- and 860-bp DNA templates with T7 promoter at the 5′ end, respectively. T7 promoter–containing DNA templates for *Mark2* and *Stxbp5* mRNA probes were transcribed by T7 RNA polymerase (Roche) in an appended transcription buffer (Roche) using the DIG RNA Labeling Mix (Roche) to yield a 559- and 833-nt digoxigenin-labeled RNA probes, respectively, which were purified in gel filtration spin columns (NucleoSEQ, MACHEREY-NAGEL). For the hybridization process, cells were fixed with 4% PFA in DEPC-treated PBS (DEPC-PBS) and permeabilized with cold methanol (1 min, 4°C) and 0.2% Triton X-100 in DEPC-PBS with 2 mM ribonucleoside vanadyl complexes (10 min, room temperature). After washing with 2× SSC buffer twice for 5 min, cells were incubated at 55°C for 15 hours with an RNA probe predenatured in hybridization buffer [2× SSC buffer containing 50% formamide, 10% (w/v) dextran sulfate, and yeast tRNA (0.1 mg/ml)]. Cells were washed three times with 2× SSC buffer containing 50% formamide, 2× SSC buffer, and 0.2× SSC buffer at 55°C and

then washed three times with PBS at room temperature. The subsequent immunochemical staining process was performed according to the standard method described in the Immunocytochemistry and immunohistochemistry section.

DNAPTP6 RIP-qPCR
RIP was performed using the RiboCluster Profiler RIP-Assay Kit (MBL) according to the manufacturer's protocol, as reported previously (57). Immunoprecipitated RNA was reverse-transcribed into single-stranded cDNA using the PrimeScript RT Reagent Kit with gDNA Eraser (Takara Bio). qPCR was performed using the following gene-specific primers: *Mark2*, GGCACCGTTCTCATCTCACA (forward) and CCTTGGTCTGAGCCATAGCC (reverse).

Preparation of *Mark2* 3′UTR mRNA and its mutants
The cDNA library was prepared using SuperScript III reverse transcriptase (Thermo Fisher Scientific) and an oligo(dT) primer from total RNAs extracted from the Neuro-2A cells. The *Mark2* 3′UTR cDNA insert was ligated to a pCAG neo vector by In-Fusion HD cloning (Takara Bio) and amplified in *E. coli* strain DH5α to obtain a pCAG-*Mark2* 3′UTR plasmid. Plasmids containing G4 deletion mutants were generated using the KOD-Plus Mutagenesis Kit (Toyobo) from the pCAG-*Mark2* 3′ UTR plasmid. T7 promoter–containing DNA templates were prepared by a standard PCR method using the PrimeSTAR Max DNA Polymerase (Takara Bio). In vitro transcription was performed using T7 RNA polymerase (Roche) in appended transcription buffer (Roche) supplemented with 2.5 mM nucleotide triphosphates (Takara Bio), RNasin Ribonuclease Inhibitor (1 U/μl; Promega), and an 800-ng DNA template at 37°C for 6 to 8 hours. For the synthesis of 7-deazaguanosine–substituted RNA, 7-deazaguanosine-5′-triphosphate (TriLink BioTechnologies) was added to the reaction instead of guanosine 5′-triphosphate (GTP) and the Ribo m7G Cap Analog (Promega). The reaction solution was treated with deoxyribonuclease I (0.08 U/μl; Thermo Fisher Scientific) at 37°C for 15 min and purified using the RNeasy Mini Kit (Qiagen). The purified *Mark2* 3′UTR RNA was capped and polyadenylated using the Vaccinia Capping System (BioLabs) and *E. coli* Poly(A) Polymerase (BioLabs), respectively, and then labeled with CX-rhodamine using the *Label* IT Nucleic Acid Labeling Kit (Mirus).

In vitro phase separation and FRAP assays
Nonlabeled proteins with specified concentrations containing 1 μM fluorescein-labeled proteins were prepared in 10 mM tris-HCl buffer (pH 7.5) containing 20 to 150 mM NaCl and 2% glycerol. RNAs with specified concentrations were refolded in 10 mM tris-HCl buffer (pH 7.5) containing 25 mM NaCl and 0 to 250 mM MgCl$_2$. For the preparation of protein/RNA complex solutions, prefolded RNAs were added to the protein solutions, which were then incubated for 10 to 30 min at room temperature. The resultant solutions were mounted on glass slides using a 0.12-nm spacer (Sigma-Aldrich) and a coverslip. Photobleaching was performed with 100% laser power to 50% intensity using the bleaching program of the ZEN software on a Zeiss LSM780 machine. Time-lapse images were recorded every 5 s using a Zeiss Objective Plan-Apochromat 63×/1.4 oil DIC M27 to track photorecovery. The fluorescent and DIC images were analyzed using the ZEN software and ImageJ. The extent to which RNAs or proteins were assembled was assessed by calculating the index of dispersion (σ^2/μ), a statistical

measure of inhomogeneity in a population, where σ^2 is the variance of the population distribution and μ is the mean value. The index of dispersion of particles in an aqueous solution should ideally be 1 if the particles follow a Poisson distribution. Biased distribution created by RNA or protein assembly exhibits a dispersion index of >1, and higher values indicate the higher rate at which RNAs or proteins are assembled and sequestered into RNA or protein condensates (40, 61). In an imaging area, fluorescence intensity per pixel was considered as the number of particles per microarea.

Patch-clamp electrophysiology

Whole-cell patch-clamp recordings were performed as previously described (24). Briefly, sEPSCs were recorded at room temperature for cultured neurons treated with or without 0.5 mM NaArs on DIV14 using an EPC10 amplifier (HEKA, Lambrecht/Pfalz, Germany). The following buffers were used: extracellular buffer (143 mM NaCl, 5 mM KCl, 2 mM CaCl$_2$, 1 mM MgCl$_2$, 10 mM glucose, and 10 mM Hepes at pH 7.4 adjusted with NaOH) and intracellular buffer (135 mM CsMeS, 5 mM CsCl, 10 mM Hepes, 0.5 mM EGTA, 1 mM MgCl$_2$, 4 mM Mg$_2$ATP, 0.4 mM NaGTP, and 5 mM QX-314 at pH 7.4 adjusted with CsOH). Recording pipettes were made of borosilicate glass (B150-86-10, Sutter Instruments) and had a resistance of 3.5 to 4.5 megohms when filled with intracellular buffer. sEPSCs were recorded for 2 min at a holding potential of -70 mV in the presence of 20 μM bicuculline in the extracellular buffer to block γ-aminobutyric acid type A receptors. Recordings were filtered at 2 kHz and digitized at 10 kHz. Access resistances were monitored throughout the experiment (<15 megohms) but not compensated. Data were collected and initially analyzed using Patchmaster software (HEKA). Further analysis was performed using SutterPatch version 2.2 (Sutter Instrument Company).

Secondary RNA structure prediction

Secondary structures of the 5′UTR or 3′UTR of *Mark2* mRNA and the 3′UTR of *Stxbp5* mRNA were predicted using the RNAstructure package (https://rna.urmc.rochester.edu/RNAstructure.html) (37). The base-pair probabilities for each RNA were calculated using the "partition" algorithm with or without single-stranded constraints at the G4 core sequences determined by the RNase T1 footprinting analysis, and the maximum pairing distance was restricted to 250 nt. Dot plot files were generated by running the "ProbabilityPlot" algorithm. Schematic RNA structure models were visualized using the Integrative Genomics Viewer (62) and *forna* (http://rna.tbi.univie.ac.at/forna/).

Statistical analysis

Comparisons between two experimental groups were made using two-sided, unpaired Student's *t* test. Statistical significance for differences among groups was tested by one-way or two-way analysis of variance (ANOVA) with post hoc Bonferroni's multiple comparison or Kolmogorov-Smirnov test. A *P* value of <0.05 was considered significant. All statistical analyses were performed using GraphPad Prism 7 (GraphPad Software).

Supplementary Materials

This PDF file includes:
Figs. S1 to S21
Table S1

View/request a protocol for this paper from *Bio-protocol*.

REFERENCES AND NOTES

1. Y. Wan, M. Kertesz, R. C. Spitale, E. Segal, H. Y. Chang, Understanding the transcriptome through RNA structure. *Nat. Rev. Genet.* **12**, 641–655 (2011).

2. H. P. Jiao, L. Wachsmuth, S. Kumari, R. Schwarzer, J. Lin, R. O. Eren, A. Fisher, R. Lane, G. R. Young, G. Kassiotis, W. J. Kaiser, M. Pasparakis, Z-nucleic-acid sensing triggers ZBP1-dependent necroptosis and inflammation. *Nature* **580**, 391–395 (2020).

3. T. Zhang, C. R. Yin, D. F. Boyd, G. Quarato, J. P. Ingram, M. Shubina, K. B. Ragan, T. Ishizuka, J. C. Crawford, B. Tummers, D. A. Rodriguez, J. Xue, S. Peri, W. J. Kaiser, C. B. Lopez, Y. Xu, J. W. Upton, P. G. Thomas, D. R. Green, S. Balachandran, Influenza virus Z-RNAs induce ZBP1-mediated necroptosis. *Cell* **180**, 1115–1129.e13 (2020).

4. R. Rangan, I. N. Zheludev, R. J. Hagey, E. A. Pham, H. K. Wayment-Steele, J. S. Glenn, R. Das, RNA genome conservation and secondary structure in SARS-CoV-2 and SARS-related viruses: A first look. *RNA* **26**, 937–959 (2020).

5. A. Cammas, S. Millevoi, RNA G-quadruplexes: Emerging mechanisms in disease. *Nucleic Acids Res.* **45**, 1584–1595 (2017).

6. M. M. Fay, S. M. Lyons, P. Ivanov, RNA G-quadruplexes in biology: Principles and molecular mechanisms. *J. Mol. Biol.* **429**, 2127–2147 (2017).

7. A. Y. Zhang, A. Bugaut, S. Balasubramanian, A sequence-independent analysis of the loop length dependence of intramolecular RNA G-quadruplex stability and topology. *Biochemistry* **50**, 7251–7258 (2011).

8. M. Malgowska, K. Czajczynska, D. Gudanis, A. Tworak, Z. Gdaniec, Overview of the RNA G-quadruplex structures. *Acta Biochim. Pol.* **63**, 609–621 (2016).

9. S. Asamitsu, Y. Yabuki, S. Ikenoshita, T. Wada, N. Shioda, Pharmacological prospects of G-quadruplexes for neurological diseases using porphyrins. *Biochem. Biophys. Res. Commun.* **531**, 51–55 (2020).

10. S. K. Mishra, A. Tawani, A. Mishra, A. Kumar, G4IPDB: A database for G-quadruplex structure forming nucleic acid interacting proteins. *Sci. Rep.* **6**, 38144 (2016).

11. C. K. Kwok, G. Marsico, A. B. Sahakyan, V. S. Chambers, S. Balasubramanian, rG4-seq reveals widespread formation of G-quadruplex structures in the human transcriptome. *Nat. Methods* **13**, 841–844 (2016).

12. J. U. Guo, D. P. Bartel, RNA G-quadruplexes are globally unfolded in eukaryotic cells and depleted in bacteria. *Science* **353**, eaaf5371 (2016).

13. Y. Katsuda, S. Sato, L. Asano, Y. Morimura, T. Furuta, H. Sugiyama, M. Hagihara, M. Uesugi, A small molecule that represses translation of G-quadruplex-containing mRNA. *J. Am. Chem. Soc.* **138**, 9037–9040 (2016).

14. S. Y. Yang, P. Lejault, S. Chevrier, R. Boidot, A. G. Robertson, J. M. Y. Wong, D. Monchaud, Transcriptome-wide identification of transient RNA G-quadruplexes in human cells. *Nat. Commun.* **9**, 4730 (2018).

15. L. T. Gray, E. P. Lombardi, D. Verga, A. Nicolas, M. P. Teulade-Fichou, A. Londono-Vallejo, N. Maizels, G-quadruplexes sequester free heme in living cells. *Cell Chem. Biol.* **26**, 1681–1691.e5 (2019).

16. M. Sauer, S. A. Juranek, J. Marks, A. De Magis, H. G. Kazemier, D. Hilbig, D. Benhalevy, X. Wang, M. Hafner, K. Paeschke, DHX36 prevents the accumulation of translationally inactive mRNAs with G4-structures in untranslated regions. *Nat. Commun.* **10**, 2421 (2019).

17. P. Murat, G. Marsico, B. Herdy, A. T. Ghanbarian, G. Portella, S. Balasubramanian, RNA G-quadruplexes at upstream open reading frames cause DHX36- and DHX9-dependent translation of human mRNAs. *Genome Biol.* **19**, 229 (2018).

18. M. M. Fay, P. J. Anderson, P. Ivanov, ALS/FTD-associated C9ORF72 repeat RNA promotes phase transitions in vitro and in cells. *Cell Rep.* **21**, 3573–3584 (2017).

19. K. M. Green, M. R. Glineburg, M. G. Kearse, B. N. Flores, A. E. Linsalata, S. J. Fedak, A. C. Goldstrohm, S. J. Barmada, P. K. Todd, RAN translation at C9orf72-associated repeat expansions is selectively enhanced by the integrated stress response. *Nat. Commun.* **8**, 2005 (2017).

20. S. K. Young, R. C. Wek, Upstream open reading frames differentially regulate gene-specific translation in the integrated stress response. *J. Biol. Chem.* **291**, 16927–16935 (2016).

21. S. Asamitsu, M. Takeuchi, S. Ikenoshita, Y. Imai, H. Kashiwagi, N. Shioda, Perspectives for applying G-quadruplex structures in neurobiology and neuropharmacology. *Int. J. Mol. Sci.* **20**, 2884 (2019).

22. R. Simone, P. Fratta, S. Neidle, G. N. Parkinson, A. M. Isaacs, G-quadruplexes: Emerging roles in neurodegenerative diseases and the non-coding transcriptome. *FEBS Lett.* **589**, 1653–1668 (2015).

23. A. R. Haeusler, C. J. Donnelly, G. Periz, E. A. Simko, P. G. Shaw, M. S. Kim, N. J. Maragakis, J. C. Troncoso, A. Pandey, R. Sattler, J. D. Rothstein, J. Wang, C9orf72 nucleotide repeat structures initiate molecular cascades of disease. *Nature* **507**, 195–200 (2014).

24. S. Asamitsu, Y. Yabuki, S. Ikenoshita, K. Kawakubo, M. Kawasaki, S. Usuki, Y. Nakayama, K. Adachi, H. Kugoh, K. Ishii, T. Matsuura, E. Nanba, H. Sugiyama, K. Fukunaga, N. Shioda, CGG repeat RNA G-quadruplexes interact with FMRpolyG to cause neuronal dysfunction in fragile X-related tremor/ataxia syndrome. *Sci. Adv.* **7**, eabd9440 (2021).

25. G. Biffi, D. Tannahill, J. McCafferty, S. Balasubramanian, Quantitative visualization of DNA G-quadruplex structures in human cells. *Nat. Chem.* **5**, 182–186 (2013).

26. S. Asamitsu, Y. Imai, Y. Yabuki, S. Ikenoshita, M. Takeuchi, H. Kashiwagi, Y. Tanoue, T. Fukuda, N. Shioda, Identification and immunohistochemical characterization of G-quadruplexes in mouse brain. *Biochem. Biophys. Res. Commun.* **531**, 67–74 (2020).

27. G. Biffi, M. Di Antonio, D. Tannahill, S. Balasubramanian, Visualization and selective chemical targeting of RNA G-quadruplex structures in the cytoplasm of human cells. *Nat. Chem.* **6**, 75–80 (2014).

28. C. J. Maltby, J. P. R. Schofield, S. D. Houghton, I. O'Kelly, M. Vargas-Caballero, K. Deinhardt, M. J. Coldwell, A 5′ UTR GGN repeat controls localisation and translation of a potassium leak channel mRNA through G-quadruplex formation. *Nucleic Acids Res.* **48**, 9822–9839 (2020).

29. A. A. Surani, C. Montiel-Duarte, Native RNA G quadruplex immunoprecipitation (rG4IP) from mammalian cells. *STAR Protoc.* **3**, 101372 (2022).

30. M. J. Lista, R. P. Martins, O. Billant, M. A. Contesse, S. Findakly, P. Pochard, C. Daskalogianni, C. Beauvineau, C. Guetta, C. Jamin, M. P. Teulade-Fichou, R. Fahraeus, C. Voisset, M. Blondel, Nucleolin directly mediates Epstein-Barr virus immune evasion through binding to G-quadruplexes of EBNA1 mRNA. *Nat. Commun.* **8**, 16043 (2017).

31. K. R. Williams, D. S. McAninch, S. Stefanovic, L. Xing, M. Allen, W. Li, Y. Feng, M. R. Mihailescu, G. J. Bassell, hnRNP-Q1 represses nascent axon growth in cortical neurons by inhibiting Gap-43 mRNA translation. *Mol. Biol. Cell* **27**, 518–534 (2016).

32. A. K. Byrd, B. L. Zybailov, L. Maddukuri, J. Gao, J. C. Marecki, M. Jaiswal, M. R. Bell, W. C. Griffin, M. R. Reed, S. Chib, S. G. Mackintosh, A. M. MacNicol, G. Baldini, R. L. Eoff, K. D. Raney, Evidence that G-quadruplex DNA accumulates in the cytoplasm and participates in stress granule assembly in response to oxidative stress. *J. Biol. Chem.* **291**, 18041–18057 (2016).

33. C. H. Zhu, J. Kim, J. W. Shay, W. E. Wright, SGNP: An essential stress granule/nucleolar protein potentially involved in 5.8s rRNA processing/transport. *PLOS ONE* **3**, e3716 (2008).

34. D. T. Jones, D. Cozzetto, DISOPRED3: Precise disordered region predictions with annotated protein-binding activity. *Bioinformatics* **31**, 857–863 (2015).

35. O. Kikin, L. D'Antonio, P. S. Bagga, QGRS Mapper: A web-based server for predicting G-quadruplexes in nucleotide sequences. *Nucleic Acids Res.* **34**, W676–W682 (2006).

36. J. M. Garant, J. P. Perreault, M. S. Scott, G4RNA screener web server: User focused interface for RNA G-quadruplex prediction. *Biochimie* **151**, 115–118 (2018).

37. J. S. Reuter, D. H. Mathews, RNAstructure: Software for RNA secondary structure prediction and analysis. *BMC Bioinform.* **11**, 129 (2010).

38. A. F. Harrison, J. Shorter, RNA-binding proteins with prion-like domains in health and disease. *Biochem. J.* **474**, 1417–1438 (2017).

39. Y. Zhang, M. Yang, S. Duncan, X. Yang, M. A. S. Abdelhamid, L. Huang, H. Zhang, P. N. Benfey, Z. A. E. Waller, Y. Ding, G-quadruplex structures trigger RNA phase separation. *Nucleic Acids Res.* **47**, 11746–11754 (2019).

40. A. Jain, R. D. Vale, RNA phase transitions in repeat expansion disorders. *Nature* **546**, 243–247 (2017).

41. S. Asamitsu, N. Shioda, Potential roles of G-quadruplex structures in RNA granules for physiological and pathological phase separation. *J. Biochem.* **169**, 527–533 (2021).

42. C. Weldon, I. Behm-Ansmant, L. H. Hurley, G. A. Burleys, C. Branlant, I. C. Eperon, C. Dominguez, Identification of G-quadruplexes in long functional RNAs using 7-deaza-guanine RNA. *Nat. Chem. Biol.* **13**, 18–20 (2017).

43. A. R. de la Faverie, A. Guedin, A. Bedrat, L. A. Yatsunyk, J. L. Mergny, Thioflavin T as a fluorescence light-up probe for G4 formation. *Nucleic Acids Res.* **42**, e65 (2014).

44. J. M. Nicoludis, S. P. Barrett, J. L. Mergny, L. A. Yatsunyk, Interaction of human telomeric DNA with *N*-methyl mesoporphyrin IX. *Nucleic Acids Res.* **40**, 5432–5447 (2012).

45. S. Jain, J. R. Wheeler, R. W. Walters, A. Agrawal, A. Barsic, R. Parker, ATPase-modulated stress granules contain a diverse proteome and substructure. *Cell* **164**, 487–498 (2016).

46. A. Khong, T. Matheny, S. Jain, S. F. Mitchell, J. R. Wheeler, R. Parker, The stress granule transcriptome reveals principles of mRNA accumulation in stress granules. *Mol. Cell* **68**, 808–820.e5 (2017).

47. H. Su, J. Xu, Y. Chen, Q. Wang, Z. Lu, Y. Chen, K. Chen, S. Han, Z. Fang, P. Wang, B. F. Yuan, X. Zhou, Photoactive G-quadruplex ligand identifies multiple G-quadruplex-related proteins with extensive sequence tolerance in the cellular environment. *J. Am. Chem. Soc.* **143**, 1917–1923 (2021).

48. B. Wolozin, P. Ivanov, Stress granules and neurodegeneration. *Nat. Rev. Neurosci.* **20**, 649–666 (2019).

49. A. L. Wolfe, K. Singh, Y. Zhong, P. Drewe, V. K. Rajasekhar, V. R. Sanghvi, K. J. Mavrakis, M. Jiang, J. E. Roderick, J. Van der Meulen, J. H. Schatz, C. M. Rodrigo, C. Y. Zhao, P. Rondou, E. de Stanchina, J. Teruya-Feldstein, M. A. Kelliher, F. Speleman, J. A. Porco, J. Pelletier, G. Ratsch, H. G. Wendel, RNA G-quadruplexes cause eIF4A-dependent oncogene translation in cancer. *Nature* **513**, 65–70 (2014).

50. S. Khateb, P. Weisman-Shomer, I. Hershco-Shani, A. L. Ludwig, M. Fry, The tetraplex (CGG)n destabilizing proteins hnRNP A2 and CBF-A enhance the in vivo translation of fragile X premutation mRNA. *Nucleic Acids Res.* **35**, 5775–5788 (2007).

51. M. Melko, B. Bardoni, The role of G-quadruplex in RNA metabolism: Involvement of FMRP and FMR2P. *Biochimie* **92**, 919–926 (2010).

52. J. B. Dictenberg, S. A. Swanger, L. N. Antar, R. H. Singer, G. J. Bassell, A direct role for FMRP in activity-dependent dendritic mRNA transport links filopodial-spine morphogenesis to fragile X syndrome. *Dev. Cell* **14**, 926–939 (2008).

53. A. Molliex, J. Temirov, J. Lee, M. Coughlin, A. P. Kanagaraj, H. J. Kim, T. Mittag, J. P. Taylor, Phase separation by low complexity domains promotes stress granule assembly and drives pathological fibrillization. *Cell* **163**, 123–133 (2015).

54. B. Tsang, J. Arsenault, R. M. Vernon, H. Lin, N. Sonenberg, L. Y. Wang, A. Bah, J. D. Forman-Kay, Phosphoregulated FMRP phase separation models activity-dependent translation through bidirectional control of mRNA granule formation. *Proc. Natl. Acad. Sci. U.S.A.* **116**, 4218–4227 (2019).

55. H. Tateishi-Karimata, N. Sugimoto, Roles of non-canonical structures of nucleic acids in cancer and neurodegenerative diseases. *Nucleic Acids Res.* **49**, 7839–7855 (2021).

56. E. Wang, R. Thombre, Y. Shah, R. Latanich, J. O. Wang, G-Quadruplexes as pathogenic drivers in neurodegenerative disorders. *Nucleic Acids Res.* **49**, 4816–4830 (2021).

57. N. Shioda, Y. Yabuki, K. Yamaguchi, M. Onozato, Y. Li, K. Kurosawa, H. Tanabe, N. Okamoto, T. Era, H. Sugiyama, T. Wada, K. Fukunaga, Targeting G-quadruplex DNA as cognitive function therapy for ATR-X syndrome. *Nat. Med.* **24**, 802–813 (2018).

58. S. Asamitsu, S. Obata, A. T. Phan, K. Hashiya, T. Bando, H. Sugiyama, Simultaneous binding of hybrid molecules constructed with dual DNA-binding components to a G-quadruplex and its proximal duplex. *Chemistry* **24**, 4428–4435 (2018).

59. Y. Katsuda, S. I. Sato, M. Inoue, H. Tsugawa, T. Kamura, T. Kida, R. Matsumoto, S. Asamitsu, N. Shioda, S. Shiroto, Y. Oosawatsu, K. Yatsuzuka, Y. Kitamura, M. Hagihara, T. Ihara, M. Uesugi, Small molecule-based detection of non-canonical RNA G-quadruplex structures that modulate protein translation. *Nucleic Acids Res.* **50**, 8143–8153 (2022).

60. R. J. Ries, S. Zaccara, P. Klein, A. Olarerin-George, S. Namkoong, B. F. Pickering, D. P. Patil, H. Kwak, J. H. Lee, S. R. Jaffrey, m(6)A enhances the phase separation potential of mRNA. *Nature* **571**, 424–428 (2019).

61. D. Tauber, G. Tauber, A. Khong, B. Van Treeck, J. Pelletier, R. Parker, Modulation of RNA condensation by the DEAD-box protein eIF4A. *Cell* **180**, 411–426.e16 (2020).

62. S. Busan, K. M. Weeks, Visualization of RNA structure models within the integrative genomics viewer. *RNA* **23**, 1012–1018 (2017).